Deep-Space Optical Communications Downlink Budget from Mars: System Parameters

A. Biswas[1] and S. Piazzolla[2]

This article describes the elements of a design control table for an optical communications link from a spacecraft in Mars orbit to a ground-based receiving station on Earth. A fixed average laser transmitter power of 5 W transmitted through a 30-cm-diameter near-diffraction-limited telescope is assumed, along with a 10-m-diameter ground receiving antenna. Pulse-position modulation of the laser with direct detection also is assumed. An end-to-end systems analysis is presented to provide the expected signal and background-noise photons as a function of the Earth–Mars range. The signal and noise photons received are treated using an ideal Poisson channel model in order to predict data rates when Mars is close to conjunction. The data rates range from 5 to 40 Mb/s with a large part of the uncertainty owing its origin to variability of the atmosphere. The article also concludes that further work is required in order to narrow the rather wide range of preliminary data rates presented.

I. Introduction

In this article, an optical communications link from a spacecraft in Mars orbit is studied with the objective of establishing preliminary bounds on the data rates achievable. A pulse-position modulation (PPM) sequence of laser pulses is transmitted to Earth, where direct detection and a ground-based receiving terminal are assumed. The transmitter diameter is 30 cm, with an average laser power of 5 W at a wavelength of 1064 nm. An effective ground-based collection aperture diameter of 10 m with an ideal photon-counting receiver is assumed.

Optical links from Mars are dominated by huge free-space propagation losses. These losses must be overcome so that sufficient laser signal photons can be reliably detected at the ground receiver while using fixed average laser power on the spacecraft. The constant average laser power, $(P_{avg})_{trans}$, of the transmitter, with a fixed pulse width, allows varying pulse energy, E_p, and pulse-repetition frequency (PRF) while satisfying the relation

$$(P_{avg})_{trans} = E_p \times PRF$$

[1] Communications Systems and Research Section.

[2] University of Southern California, Los Angeles, California.

The research described in this publication was carried out by the Jet Propulsion Laboratory, California Institute of Technology, under a contract with the National Aeronautics and Space Administration.

So, at the longest ranges, pulses with sufficient energy to overcome the losses are transmitted to achieve data rates commensurate with the PRF that can be supported. As range decreases, progressively increasing data rates can be realized. Thus, channel capacity (bits/second) is traded for channel efficiency (bits/photon) as the communications range increases.

PPM lends itself elegantly to this direct-detection scheme. The emitted laser pulse is positioned in one of M time slots, each T_s seconds wide, in order to encode $\log_2 M$ bits of data per PPM symbol. The product of slot width, T_s, and M defines the symbol duration. In the analysis to be presented, fixed slot widths of 2 ns are considered. In future articles, variable slot widths will be analyzed. The effect of an upper bound on the PPM order also is considered.

The communications link equation determines the relation between mean received signal power, $(P_{avg})_{recd}$, and transmitted power, $(P_{avg})_{trans}$:

$$(P_{avg})_{recd} = (P_{avg})_{trans} \times G_T \times \eta_T \times L_{TP} \times L_s \times \eta_{atm} \times \eta_R \times G_R \times L_{\text{other}} \tag{1}$$

where

$G_{T,R} =$ the transmitter and the ground-receiver gain

$L_{TP} =$ the loss allocated for imperfect pointing of the narrow laser beam

$L_S =$ the free-space loss

$L_{\text{other}} =$ a miscellaneous loss term explained below

$\eta_{(T,atm,R)} =$ the transmitter, atmospheric, and receiver efficiencies at the laser wavelength

For this preliminary report, an ideal photon-counting receiver is considered. Future articles will address deviations expected from this model when realistic device constraints are accounted for. The average received signal power is converted to detected signal photons, n_s, after scaling with the quantum efficiency of the detector. Even though narrow bandpass optical filters are used to reject out-of-band background-noise photons, an in-band fraction contributed by sunlight scattered and reflected by the sky and Mars will be incident upon the detector. The number of background-noise photons is directly proportional to the detector field of view or solid angle used. Furthermore, in-band noise photons from outside the detector field of view, referred to as stray light, also may contribute to background noise. The aggregate of background-noise photons scaled by the quantum efficiency results in n_b detected noise photons. Treating the $n_s + n_b$ detected photons by a Poisson [1,2] process allows a determination of the channel capacity. A companion article [3] details the derivation of realizable data rates, given a combination of n_s and n_b. Synchronization and quantization losses of 1 dB together with a link margin of 3 dB and a coding gap of 0.75 dB are taken. Thus, a net reduction of 4.75 dB from capacity is used to estimate the realizable data rates. The remainder of this article will emphasize the estimation of n_s and n_b for a Mars downlink.

In Section II, a typical Mars mission profile is described, using planned Mars Telecom spacecraft cruise data. Section III describes the downlink budget allocations and how they are combined to determine the average received signal photons under a variety of conditions. Section IV provides a detailed description of background noise, and Section V discusses the achievable data rates when Mars is at its farthest range and presents the ground receiver with a small Sun–Earth–probe angle. Finally, in Section VI, some conclusions and directions for future work are indicated.

II. Mars Mission Profile

The Mars Laser Communications Demonstration (MLCD) planned to fly onboard the Mars Telecom Orbiter (MTO) spacecraft, with a planned launch date of October 2009 and arrival at Mars in August 2010, is used as an example. Figure 1(a) shows the range, while Fig. 1(b) shows the variation of

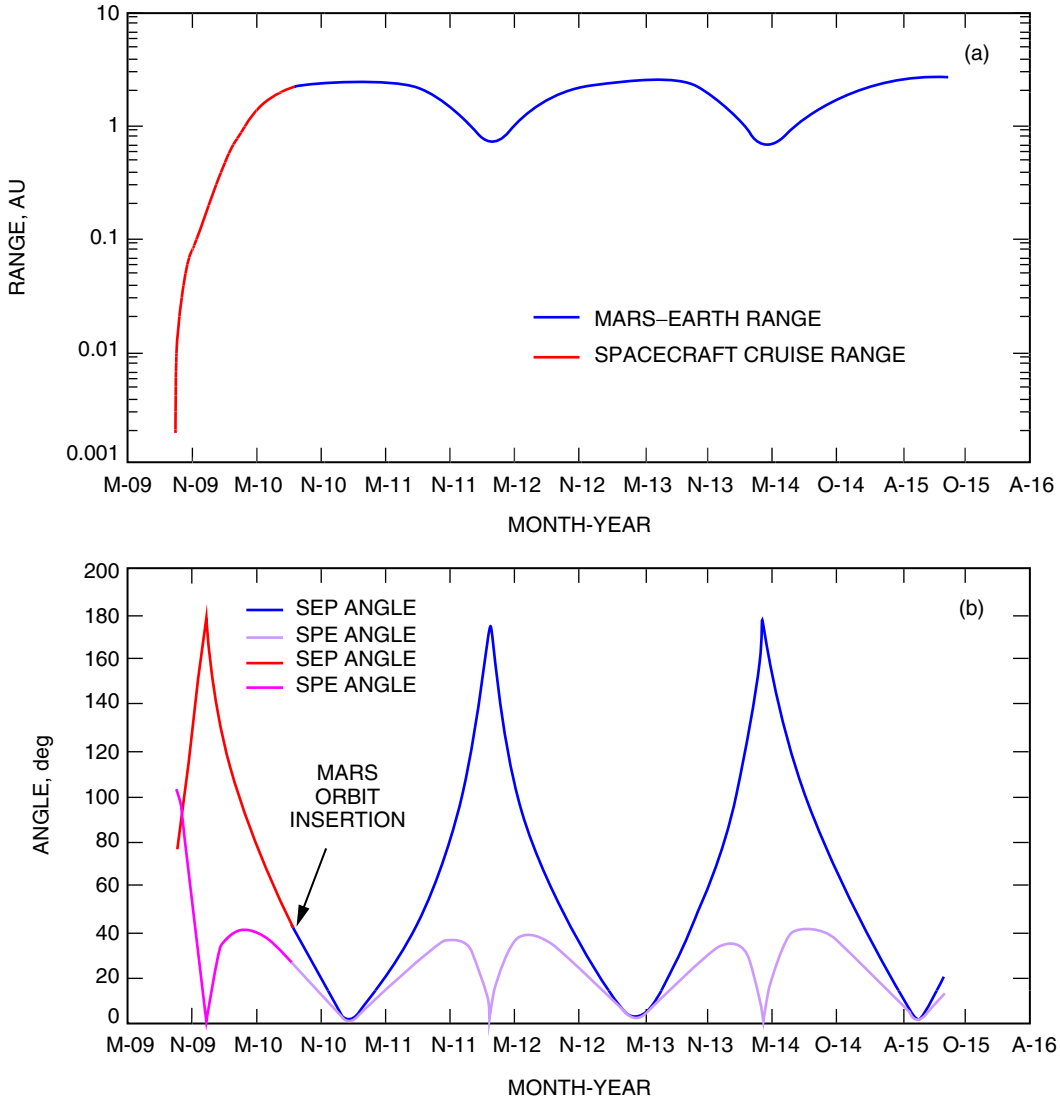

Fig. 1. Mars Telecom Orbiter: (a) range as a function of time starting with launch and 5 years after Mars orbit insertion and (b) the SEP and SPE angles for MarsTelecom. The cruise phase uses mission ephemeris, whereas Mars ephemeris data are used to approximate the range and Sun angles following orbit insertion.

Sun angle, Sun–Earth–probe (SEP) and Sun–probe–Earth (SPE), with time. The latest available data for the cruise phase of Mars Telecom have been used, whereas, following orbit insertion, the spacecraft is approximated by the planet Mars' range and Sun angles. At Earth–Mars conjunction, the orbital geometry causes the Earth–Mars range to reach a maximum as the SEP and SPE angles reach their minima. Therefore, the space transmitting and Earth receiving terminals must both point close to the Sun when Mars is at maximum range.

Figure 2 shows a histogram of the number of days spent at small SPE/SPE angles during Earth–Mars conjunction. The number of days can be interpreted as the outage duration that would result for the corresponding SEP/SPE angle cut-off; for example, for an SPE angle cut-off of 2 degrees, there will be approximately 22 days of outage. Likewise, Fig. 2(b) shows the days spent at small SPE angles during Mars opposition. Note that at opposition the range to Mars is minimum and the Earth terminal is pointing at the night sky while the space terminal is pointing back at Earth with angular separation between the Sun and Earth being very small.

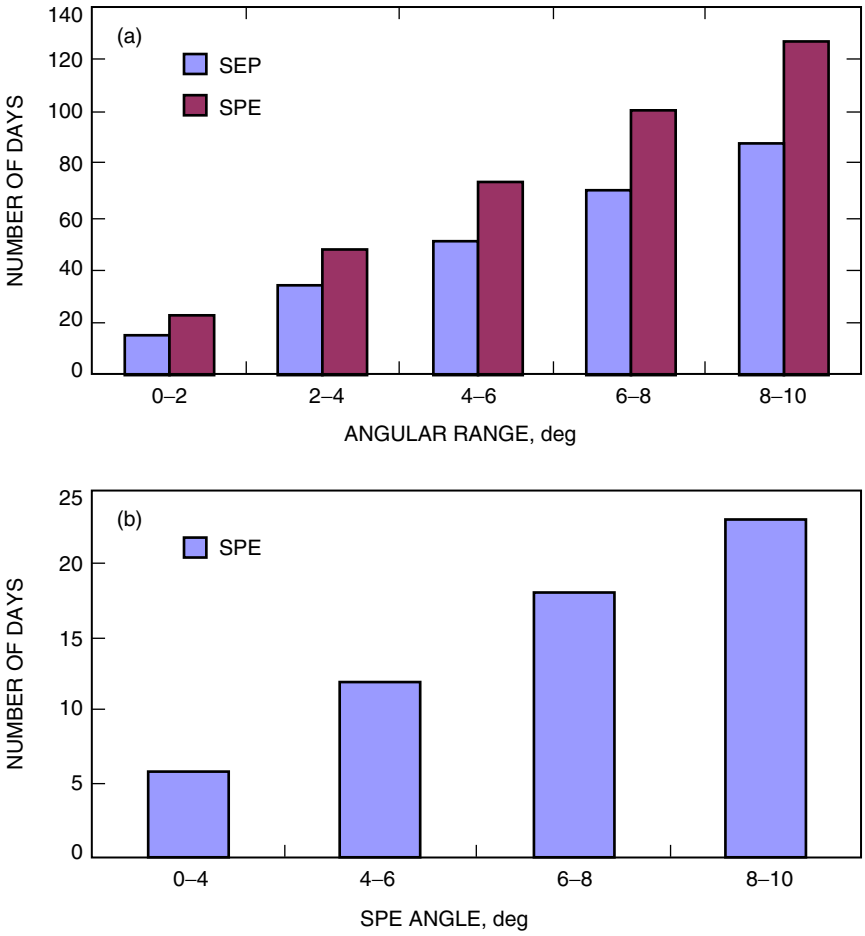

Fig. 2. Sun-angle constraints at Earth–Mars conjunction: (a) days spent at Sun angles <10 deg during Mars–Earth conjunction and (b) days spent at small SPE angles during Mars–Earth opposition.

The mission profiles summarized in Fig. 1 give an indication of the long-term variation in range and background noise on the optical link. Figure 3 shows the daily variation in elevation and azimuth angles, for example, as Mars is observed from Table Mountain, California. Here the daily or short-term variation in link geometry is shown for a few representative passes spanning one Mars orbital cycle. As elaborated in Section IV, these daily variations affect the atmospheric attenuation and sky background noise.

III. Downlink Budget Allocations

A. Downlink Budget Flow Chart

The downlink budget from Mars was determined using the scheme graphically summarized in Fig. 4(a). Constant average power from the laser on the spacecraft is obtained, with an expected electrical-to-optical conversion efficiency of 10 to 12 percent. Following system losses, the laser beam propagates through space towards the ground-based Earth receiver, undergoing pointing and space losses. Sunlight reflected from Mars and starlight integrated over the same solid angle as the laser signal also is present. The laser beam incident upon Earth's atmosphere is a plane wave; however, the interaction with the turbulent atmosphere results in phase distortions and attenuation losses. The phase-distorted or "speckle" laser beam is incident upon the receiver aperture on the ground. In addition to Mars and starlight, sunlight

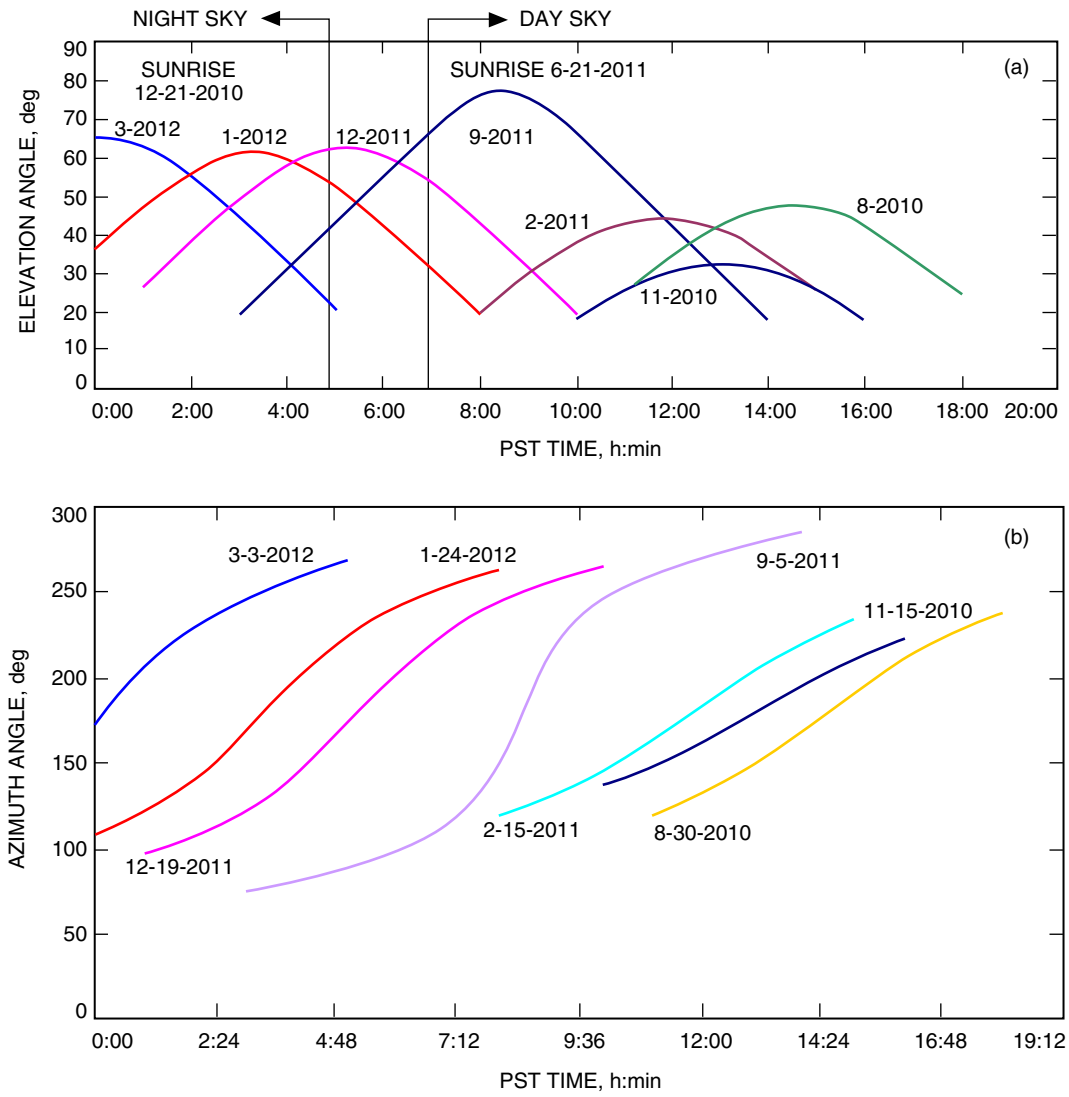

Fig. 3. Ephemeris predictions for several Mars passes as observed from Table Mountain, California: (a) elevation angle versus time of day and (b) azimuth angle versus time of day.

scattered by the atmosphere also finds itself at the receiver aperture along with stray light. Equation (1) describes the net losses experienced by the laser transmitted from the spacecraft. In addition, in-band or background-noise photons with the same wavelength as the signaling laser are simultaneously received. The M-PPM slot width and detector quantum efficiency convert the received photon flux into detected signal and noise photons per slot. The resulting average signal per slot, n_s/M, and noise, n_b, provide an operating point for the link. The dashed line labeled Doppler shift in Fig. 4(a) is included as a reminder that the laser wavelength received will undergo shifts, and this must be accounted for in the optical filtering that is performed to reject out-of-band background photons from reaching the detector.

The system throughput is determined by fixed and variable gain and loss components, listed in Fig. 4(b). Fixed components comprise transmitter gain, G_T; transmitter efficiency, η_T; pointing losses, L_{RP}; and receiver losses, η_R, while the variable components comprise space loss, L_S, and atmospheric attenuation, η_{atm}. Receiver gain, G_R, usually fixed for a given point design, is treated as a variable quantity in this article in order to evaluate and compare the link using variable antenna aperture diameters.

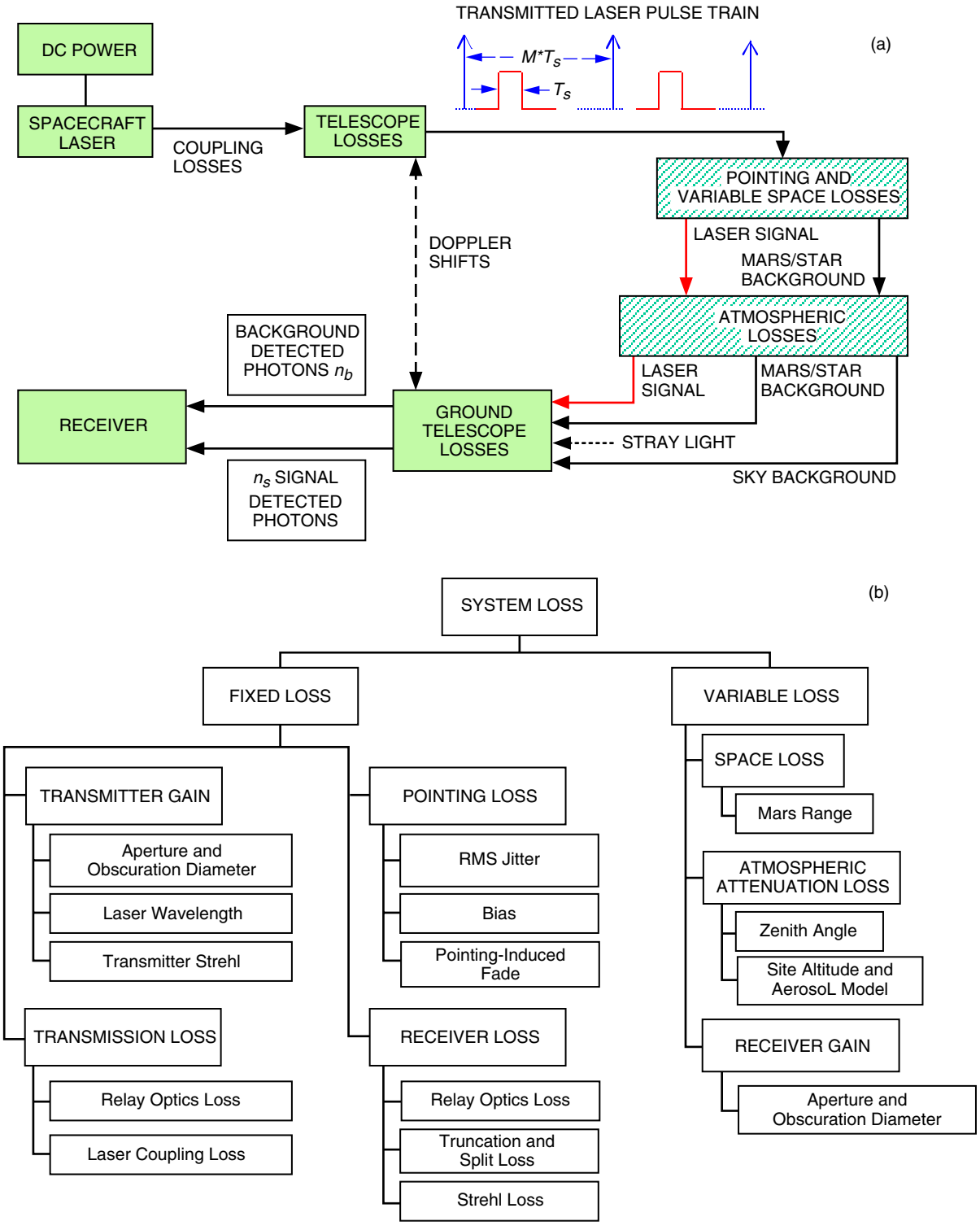

Fig. 4. Downlink budget: (a) a schematic representation of the parameters involved in deriving signal, n_s, and noise, n_b, photons incident on the detector and (b) classification scheme for the system losses experienced by a deep-space optical link.

B. Fixed System Losses

1. Transmitter Gain. Transmitter gain is defined as [4]

$$G(r_1, \theta_1) = \frac{I(r_1, \theta_1)}{I_0} \tag{2}$$

or the ratio of the intensity radiated in the direction of the telescope optical axis, $I(r_1, q_1)$, over that for a unity power isotropic radiator, I_0, with

$$I_0 = \frac{1}{4\pi r_1^2} \tag{3a}$$

and

$$I(r_1, \theta_1) = \frac{k^2}{r_1^2} \left| \int_b^a \sqrt{\frac{2}{\pi}} \frac{1}{\omega} \exp\left(-\frac{r_0}{\omega^2}\right) \exp\left[j \frac{k r_0^2}{2} \left(\frac{1}{r_1} + \frac{1}{R}\right)\right] J_0(k r_0 \sin\theta_1) r_0 dr_0 \right|^2 \tag{3b}$$

where k is the wavenumber $(2\pi/\lambda)$ for a laser wavelength, λ; r_1, θ_1 are the observation point; ω is the $1/e^2$ radius of the Gaussian beam being coupled to the telescope optics; and R is the radius of curvature of the beam front at the telescope aperture plane. The geometry of the incoming laser, assumed to be a TEM00 single spatial-mode beam with respect to the telescope optics, is shown in Fig. 5. The $1/e^2$ Gaussian width, ω, of the laser beam overfills the telescope aperture with radius a. The quantity $\alpha = a/\omega$ quantifies

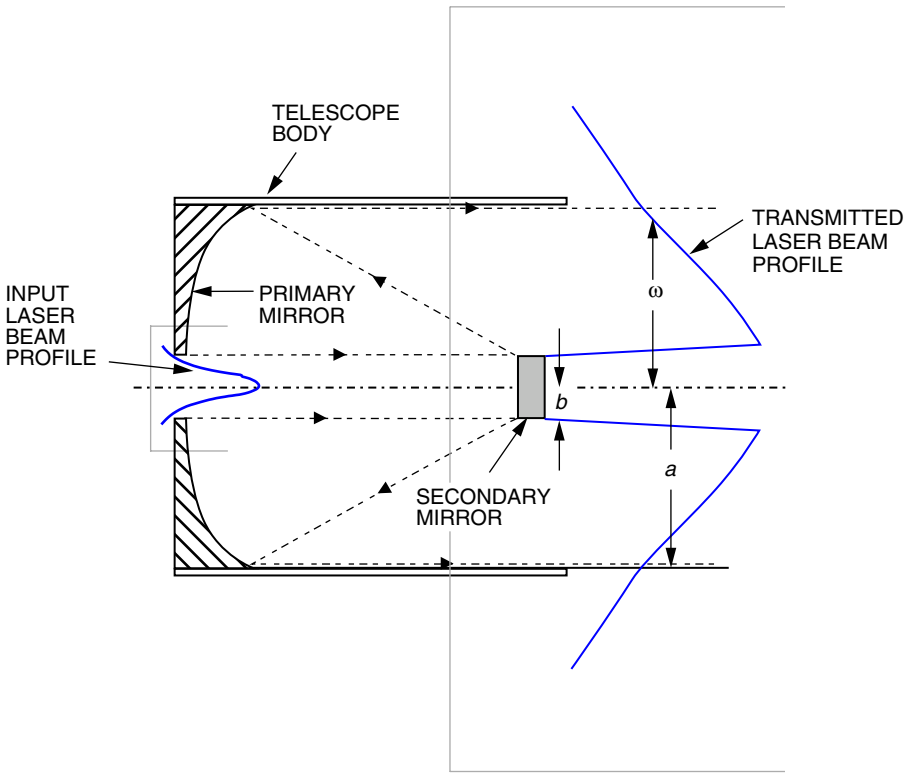

Fig. 5. The relation between a Gaussian profile laser beam and a transmitting telescope.

the resulting truncation loss. In addition, there is an obscuration loss characterized by the parameter $\gamma = b/a$, with a and b representing the radius of the primary and secondary mirrors. In the present analysis, vignetting losses that may arise from the incoming laser beam overfilling the central hole in the primary mirror are neglected. The transmitter gain can be reduced to the equation [4]

$$G_T(\alpha, \beta, \gamma, X) = \left(\frac{4\pi A}{\lambda^2}\right) g_T(\alpha, \beta, \gamma, X) \tag{4}$$

with $\beta = (ka^2/2)[(1/r) + (1/R)]$ and $X = ka \sin\theta_1$. Thus, the theoretical transmitter gain factor can be a maximum of $(4\pi A/\lambda^2)$, the ideal unobscured antenna gain, with A being the area of the primary while the term g_T represents a transmitter efficiency factor that can be defined by the equation

$$g_T(\alpha, \beta, \gamma, X) = 2\alpha^2 \left| \int_{\gamma^2}^{1} \exp(j\beta u) \exp(-\alpha^2 u) J_0\left[X(u)^{1/2}\right] du \right|^2 \tag{5}$$

Substituting $\beta = 0$ for far-field gain and $X = 0$ for on-axis gain, the transmitter efficiency term can be simplified to

$$g_T(\alpha, 0, \gamma, 0) = \frac{2}{\alpha^2}\left[\exp(-\alpha^2) - \exp\left(-\gamma^2\alpha^2\right)\right] \tag{6a}$$

and it can further be shown that optimal transmitter efficiency is obtained by satisfying the approximate relation

$$\alpha \approx 1.12 - 1.30\gamma^2 + 2.12\gamma^4 \tag{6b}$$

Equation (6b) is reported to be reliable within ±1 percent for $\gamma \leq 0.4$. Thus, for $\gamma = 0$, a ratio of 1.12 of the aperture and beamwidth will optimize the transmitter gain efficiency.

Theoretically, for a 0.3-m-aperture telescope transmitting a laser with $\lambda = 1.064$ μm, the ideal unobscured gain is $10^* \log(4\pi A/\lambda^2)$, which is 118.95 dB. The on-axis transmit efficiency, Eq. (6a), is plotted in Fig. 6 for a number of different obscuration ratios. Even for an unobscured aperture, the theoretical maximum gain is reduced due to truncation.

The spatial distribution of the gain efficiency factor in the far field ($\beta = 0$) is calculated using the integral of Eq. (5). Figure 7 shows this distribution added to the idealized unobscured gain term as a function of the radial angle expressed as $(\theta \times D/\lambda)$ so that the numbers can be expressed in units of λ/D, where $D = 2a$ is the diameter of the transmitting aperture. These gain distributions provide the angular beamwidth Θ, which can be defined in a number of ways. Table 1 lists the half-angular width to the first null, Θ; the $1/e^2$ width, $\Theta_{8.7\text{dB}}$; and finally the full-width at half-maximum (FWHM), $\Theta_{3\text{dB}}$, along with some other parameters of interest for transmitting a laser beam through a circular aperture. With increasing obscuration, the antenna gain reduces and the beam also gets narrower. For most cases of interest, $\Theta_{3\text{dB}}$ is the beamwidth of interest as the laser communication system will always try to keep the beam mispointing losses to a fraction of this quantity, as described in the next section.

The results discussed so far apply to the case where α is chosen to be optimal. Figure 8(a) shows the effect of varying α with γ fixed at 0.1. As expected, the on-axis gain decreases as the α deviates from the optimal value of 1.1. Furthermore, as α exceeds the optimal value, or equivalently as the Gaussian width, ω, decreases, the beamwidth increases with a decrease in gain. On the other hand, if α is less

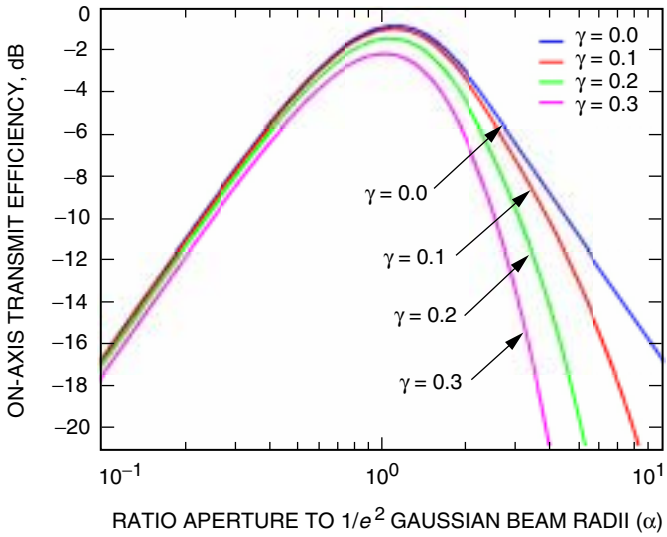

Fig. 6. The variation in the transmit efficiency with $\alpha = a/\omega$. For a given obscuration, there is an optimal value of α that provides a maximum transmit efficiency.

than optimum, meaning an increase in ω, there is a more rapid decrease in gain, due to the more severe truncation, with a reduction in angular beamwidth. The $\Theta_{3\mathrm{dB}}$ dependence on α is shown in Fig. 8(b), where the nontruncated Gaussian beamwidth defined as $\lambda/(2 \times \omega)$ is also shown for comparison. Thus, it appears that the truncation of a Gaussian TEM00 beam by an aperture alters the far-field beamwidth depending upon the ratio of the aperture radius to the Gaussian $1/e^2$ waist size.

The preceding discussion of transmitter gain was premised upon a perfect optical system. The effective optical wave-front error (WFE) or Strehl ratio [5] perturbs the achievable gain and beamwidth. The effect of a Strehl ratio S being less than 1, indicating a less-than-perfect wave-front-quality optical system, is a reduction in on-axis gain with a simultaneous broadening of the angular beamwidth that can be approximated by using the factor $1/\sqrt{S}$. Table 2 lists the achievable gains and beamwidths that take into account a less than perfect value of S.

Materials like SiC are highly sought after for optical communications flight terminals because of their light weight combined with stiffness and thermal stability. However, realizing perfect optical quality with these materials is not trivial. Figure 9 shows the cost versus Strehl for a SiC telescope based upon data provided by SSG Inc. The cost assumes a single deliverable flight telescope and includes and nonrecurring (NRE) costs. The plot is for a 30-cm off-axis three-mirror anastigmat afocal telescope with appropriate folding. The Strehl includes telescope operational performance in a space environment but does not include contributions from the back-end optics. The operating temperature for such a telescope would be −40 deg C to +50 deg C. The increase in cost shown at a Strehl of 0.87 represents the practical difficulty in delivering a better optical performance. Obviously, for a flight terminal the very best possible gain will be desired and sought; however, Fig. 9 points out some of the practical constraints.

To summarize, best-, nominal-, and worst-case transmitter gains can easily be chosen from the data provided in Table 2. Accompanying the choice of gain is an angular beamwidth that is going to dictate the performance of the pointing control system; this is elaborated on in the next section.

2. Pointing Loss. In the preceding section, the on-axis transmitter gain and angular beamwidth were determined. Any mispointing of the laser beam that causes the receiver to be located off-axis from the far-field irradiance profile will result in a loss. This is called a pointing loss. Furthermore, keeping the

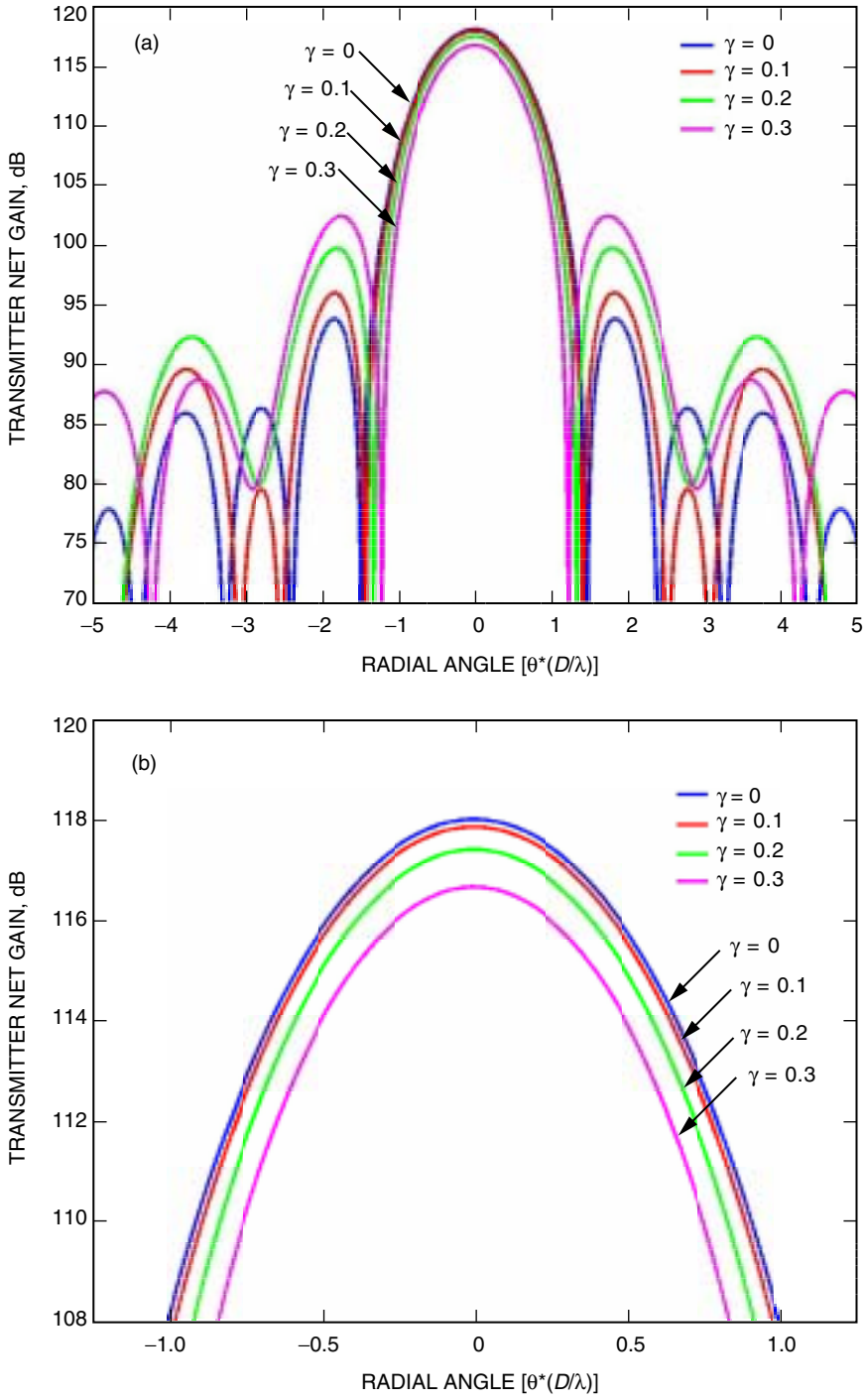

Fig. 7. The far-field (a) transmitter gain distribution; the ordinate represents the number of dB that the gain will drop with off-pointing when the α is optimized according to Eq. (6b) and (b) an expanded view showing the gain distributions of Fig. 7(a) with the $1/e^2$ angular widths indicated in Table 1.

Table 1. List of parameters transmitting a truncated Gaussian laser beam through an annular aperture.

Obscuration ratio γ	Optimal α	Peak transmit efficiency g_T, dB	Net transmit gain G_T, dB	Θ, full-angular width to null $[\theta \times (D/\lambda)]$	$\Theta_{8.7\text{dB}}$, full $1/e^2$ (−8.7 dB from peak), angular width $[\theta \times (D/\lambda)]$	$\Theta_{3\text{dB}}$ FWHM (−3 dB from peak), angular width $[\theta \times (D/\lambda)]$
0.0	1.1200	−0.89	118.10	2.96	1.88	1.16
0.1	1.1072	−1.04	117.80	2.86	1.86	1.14
0.2	1.0714	−1.50	117.45	2.66	1.76	1.10
0.3	1.0202	−2.24	116.70	2.44	1.68	1.06

narrow-angular-width laser beam pointed in the presence of spacecraft attitude and vibration disturbances becomes a formidable challenge. Therefore, in determining a link budget, some losses are allocated to mispointing.

In Fig. 10, the loss of gain as a function of mispointing is plotted for a 30-cm telescope with varying obscuration ratios ranging from 0 to 0.3. This plot assumes a perfect optical system. Note that while Table 2 approximates the effect of Strehl on gain and beamwidth, the proper analysis to assess the effect of Strehl on the distribution shown in Fig. 10 is beyond the scope of the current article. Figure 10 does show that the 2-dB loss will involve a mispointing of 1.54 to 1.69 μrad and, for a 1.25-dB loss, the mispointing will further reduce to 1.23 to 1.34 μrad. Increasing the obscuration ratio γ appears to reduce the tolerable mispoint angle for a fixed-loss allocation. Degrading the Strehl ratio for any γ also will have a similar effect, namely, the tolerable angular mispoint angle for a fixed loss will increase although the peak gain itself will decrease with Strehl.

As reported previously [6], the probability distribution function for pointing errors can be expressed as the Rice density:

$$p(\theta_e) = \frac{\theta_e}{\sigma^2} \exp\left[-\frac{1}{2\sigma^2}\left(\theta_e^2 + \eta^2\right)\right] I_0\left(\frac{\theta_e \eta}{\sigma^2}\right) \tag{7}$$

Here θ_e is the pointing error comprised of orthogonal Cartesian components θ_x and θ_y, with

$$\theta_x = \theta_e \cos(\varphi)$$

and

$$\theta_y = \theta_e \sin(\varphi)$$

with

$$\varphi = \tan^{-1}\left(\frac{\theta_y}{\theta_x}\right)$$

Furthermore, θ_x and θ_y are independent random variables with mean η_x, η_y, variance σ_x, σ_y, a radial mean defined as $\eta = \left[\eta_x^2 + \eta_y^2\right]^{1/2}$, and an angular variance $\sigma^2 = \sigma_x^2 = \sigma_y^2$. I_0 is the modified zero-order

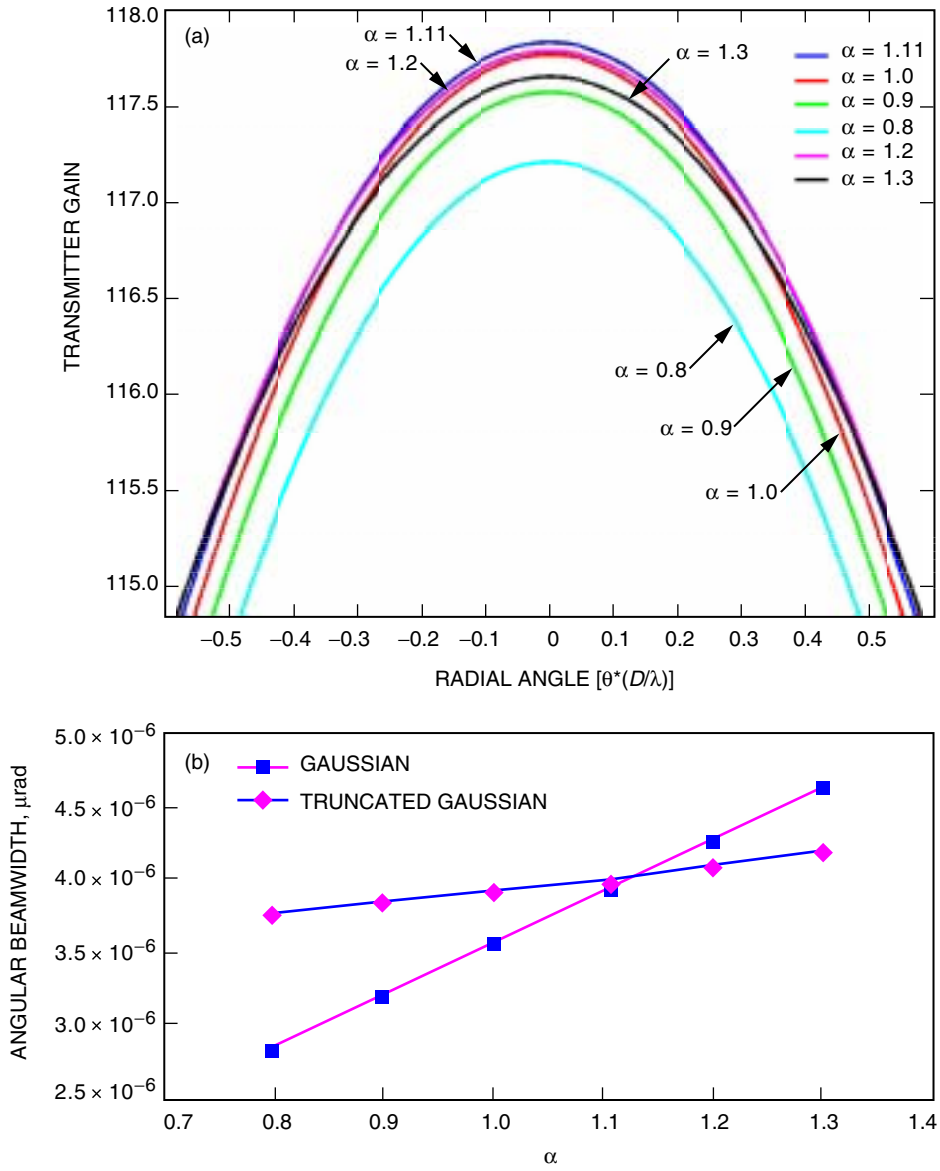

Fig. 8. Estimation of far-field beamwidth as the ratio of Gaussian beamwidth to aperture diameter is varied: (a) the effect of varying α on far-field gain profile for a $\gamma = 0.1$ and (b) the Θ_{3dB} dependence upon the ratio of aperture radius to the Gaussian $1/e^2$ beam radius, compared to the angular beamwidth of a nontruncated Gaussian beam.

Bessel function. Thus, given a pointing-loss allocation, the probability that the pointing will exceed the allocation or a pointing-induced fade (PIF) can be determined by an integration of Eq. (7):

$$PIF = \int_{\delta}^{\infty} p(\theta_e) d\theta_e \tag{8}$$

Note that $\eta + 3\sigma \leq \delta$ in order to stay within the pointing allocation and that PIF gives the probability that this condition will be violated. Different combinations of bias and jitter can be used to satisfy the 2-dB pointing-loss allocation. For example, choosing $\eta = 0.36$ μrad and $\sigma = 0.36$ μrad for the current

Table 2. Variation of far-field gain for a truncated Gaussian laser beam transmitted through an annular aperture.

Obscuration ratio	$S = 1$		$S = 0.9$		$S = 0.8$	
	Gain, dB	Θ_{3dB}, μrad	Gain, dB	Θ_{3dB}, μrad	Gain, dB	Θ_{3dB}, μrad
0.0	118.1	4.11	117.6	4.34	117.1	4.60
0.1	117.8	4.04	117.3	4.26	116.8	4.52
0.2	117.5	3.90	117	4.11	116.5	4.36
0.3	116.7	3.76	116.2	3.96	115.7	4.20

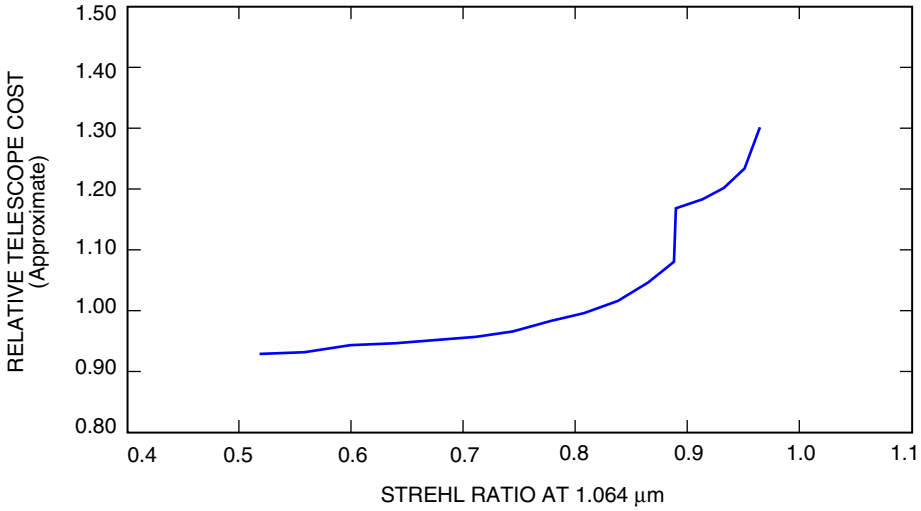

Fig. 9. The cost versus Strehl for a SiC space telescope.

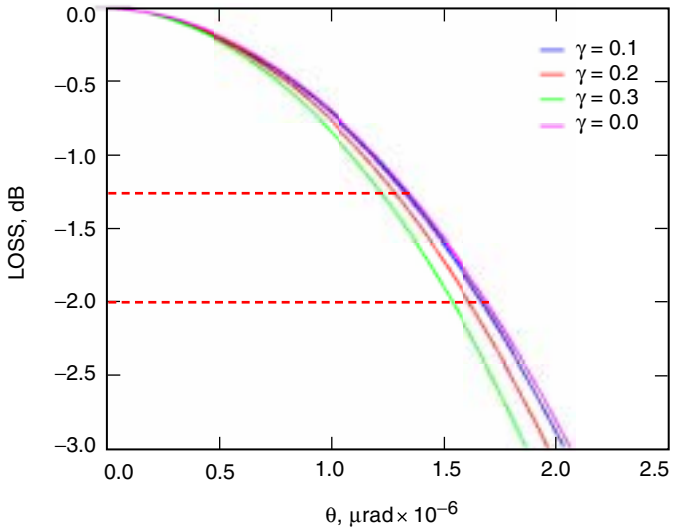

Fig. 10. The loss in gain due to mispointing of the beam.

Mars link budget yields the probability distribution function shown in Fig. 11. Using Eq. 8 yields a corresponding PIF of 0.0012 or 0.12 percent. So, provided the pointing bias and jitter can be held within the allocation, then 99.88 percent of the time the beam will be pointed in a manner that will result in $\leq$2-dB loss.

3. System Efficiency. The transmitter throughput relates to the fraction of emitted laser power that exits the telescope. Generally the losses can be subdivided into (1) those incurred in coupling the laser beam to the telescope optical system and (2) transmit losses in propagating through the telescope optical system.

For fiber lasers, the output must be collimated and matched to the telescope optical system. On the other hand, when a free-space coupled laser with a TEM00 output is used, it may have to be recollimated to match the telescope optical system. In either case, some coupling losses will be incurred. Four to six anti-reflection-coated optical surfaces are assumed with a 3 to 5 percent allocation to vignetting and another 2 to 5 percent allocated for scattering losses.

The transmission efficiency on the other hand assumes 7 to 8 anti-reflection-coated surfaces, with a 3 to 5 percent allocation for polarization, vignetting, and scatter losses. The vignetting losses here take into account the loss from supporting struts on the transmitting telescopes. The loss contributions are listed as "worst" and "best" cases in Table 3.

Table 3 also lists the losses associated with receiving the laser signal. A single-aperture collection system is assumed with a primary and secondary or corrector element. We assume 5 to 15 percent primary- and secondary-mirror losses. Transmission losses through a narrow bandpass optical filter with 80 to 90 percent efficiency and tuned to the center of the laser spectral line are budgeted next. Relay optics transmission of 70 to 85 percent is assumed. The laser signal will undergo truncation loss associated with the laser focal spot overfilling the detector area. As discussed in Section IV, this is related to atmospheric seeing, and a 30 percent loss in signal energy is assumed. This accounts for the blur circle overfilling the detector area, which is chosen to be 80 percent of the blur-circle size, and an additional 10 percent allocation attributed to imperfect tracking of the spacecraft by the telescope. Note the sacrifice of 20 percent of the signal energy actually results in a net improvement in signal-to-noise ratio because, as shown later, a large amount of background light is rejected in the process.

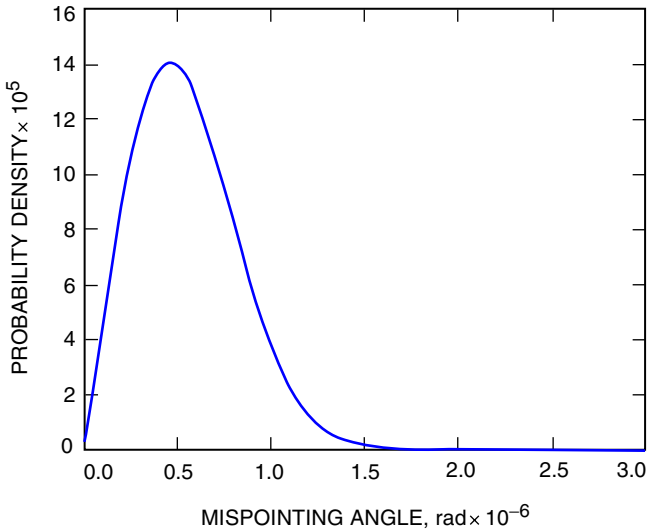

Fig. 11. PDF as a function of the mispointing angle for a fixed bias and rms jitter that is 10 percent of the mispointing angle required for a 2-dB loss.

Table 3. Summary of transmit and receive losses in dB for the downlink laser.

Transmitter efficiency	Worst, dB	Best, dB
Laser coupling loss		
4–6 AR-coated surfaces	−0.53	−0.35
Scatter losses	−0.22	−0.13
Vignetting losses	−0.22	−0.09
Subtotal	−0.97	−0.57
Transmission efficiency		
8 AR-coated surfaces	−0.70	−0.46
Polarization losses	−0.22	−0.13
Vignetting losses	−0.22	−0.13
Scattering losses	−0.22	−0.13
Subtotal	−1.37	−0.86
Total transmitter efficiency	−2.34	−1.43
Receiver optical efficiency	**Worst, dB**	**Best, dB**
Primary mirror	−0.71	−0.22
Secondary or corrector	−0.71	−0.22
Filter	−0.97	−0.46
Relay optics	−0.68	−1.59
Truncation loss	−1.55	−1.55
Polarization losses	−0.97	−0.46
Total receiver optical efficiency	−5.58	−4.50

Finally, a 10 to 20 percent polarization loss is assumed; this loss is incurred by the circularly polarized laser beam due to depolarization from reflections as well as transmission through the polarizing optics. However, the signal energy sacrificed to the polarizer is a worthwhile trade since the polarizing optics reject 50 percent of the unpolarized background light from all sources. Table 3 summarizes all the worst- and best-case loss estimates.

C. Variable System Losses

1. Space Loss. The space loss is given by

$$L_s = \frac{\lambda}{4\pi R^2} \tag{9}$$

where R represents the distance between the transmitter and receiver. The space loss, therefore, varies as the range varies according to Fig. 1(a). Table 4 lists the maximum and minimum space loss in dB during different phases of the mission.

2. Receiver Gain. In this article, the receiver gain is treated as a variable quantity so that several different ground receiving systems can be evaluated and compared. The receiver gain is given by the simple expression [7]

$$G_R(\text{dB}) = 10\log\frac{4\pi A}{\lambda^2} + 10\log(1-\gamma^2) \tag{10}$$

with A being the area of the primary mirror of the receiving antenna. Table 5 shows some of the ground-based telescopes considered as potential assets for receiving the laser signal transmitted form Mars. The first entry in Table 5 is a hypothetical 10-m-diameter segmented array described in [8].

3. Atmospheric Attenuation. Atmospheric attenuation losses vary on a much shorter term as the zenith angle to the spacecraft varies over the duration of a pass, typically 6 to 9 hours. There will be variation due to the dependence of attenuation upon the zenith angle that varies continuously during a pass (see Fig. 3). In addition, day-to-day fluctuations in atmospheric conditions will also give rise to variable attenuation, but those are not considered here. Table 6 provides representative attenuations predicted using a software tool called MODTRAN [9]. Zenith angles from the ground receiver perspective of 0 deg and 70 deg with a variety of assumptions for the atmosphere are given. As shown, atmospheric attenuation could span quite a range, which includes regions over which links are viable to adverse conditions where communications outages are encountered. The disadvantage of utilizing ground-based receivers at sea level is clearly emphasized in Table 6, where it is shown that cirrus clouds could cause as much as 8 dB of attenuation that will most likely result in a link outage.

Table 4. Range of space losses expected during different phases of the Telecom mission.

Mission phase	Space loss, dB
Cruise (assume 120 days after launch for minimum range)	−355.6 to −371.5
Orbit 8/30/2010 to 8/30/2012	−361.5 to −372.5

Table 5. A selection of potential ground telescopes that could be used as receiving antennas for a Mars optical link.

Telescope	D, m	Obscuration, m	Nominal gain, dB
Hypothetical	10	1.4	149.3
Keck, Mauna Kea	10	0.2	149.3
Palomar	5	1	143.2
AEOS (Advanced Electro-Optical System), Mt. Haleakala	3.67	0.86	140.5
IRTF (Infrared Telescope Facility), Mauna Kea	3	0.9	138.9
Hooker Telescope, Mt. Wilson	2.5	—	—
TMF	1	0.2	129.3

Table 6. Representative attenuations predicted using MODTRAN.

Atmospheric model	Zenith attenuation, dB			70-deg attenuation, dB		
	0 km	2 km	3 km	0 km	2 km	3 km
Desert extinction	−0.23	−0.16	−0.14	−0.67	−0.49	−0.4
23-km visibility, no clouds	−0.60	−0.22	−0.11	−2.06	−0.65	−0.32
5-km visibility with high cirrus clouds	−2.75	−0.81	−0.73	−8.10	−2.37	−2.14

IV. Background-Noise Estimation

Figure 12 shows a flowchart of the steps used to estimate detected background-noise photons, η_b. Background noise is largely rejected by the use of optical narrow bandpass filters (NBPFs); however, the in-band fraction contributes a significant number of photons. All background light sources within the detector field of view (FOV) contribute to noise; furthermore, stray-light infiltration from beyond the FOV is possible.

A. Atmospheric Seeing Effects

Daytime background sky noise is of particular concern when sunlight undergoing multiple scattering by atmospheric constituents impinges upon the detector. The amount of background contributed by the sky is proportional to the FOV or, equivalently, the solid angle subtended on the detector. A minimum solid angle, set by the severity of atmospheric turbulence, as elaborated below, must be maintained in order to ensure adequate laser-signal collection. Physically the plane wave front of the laser beam transmitted from space is broken up by random refractive-index perturbations of the atmosphere. The extent of the fluctuations is determined by the severity of atmospheric turbulence. The so-called atmospheric coherence diameter or Fried parameter [10], r_0, represents the spatial extent over which the phase front of an optical beam is preserved. The more turbulent the atmosphere gets, the smaller r_0 will be. Compared to a perfect

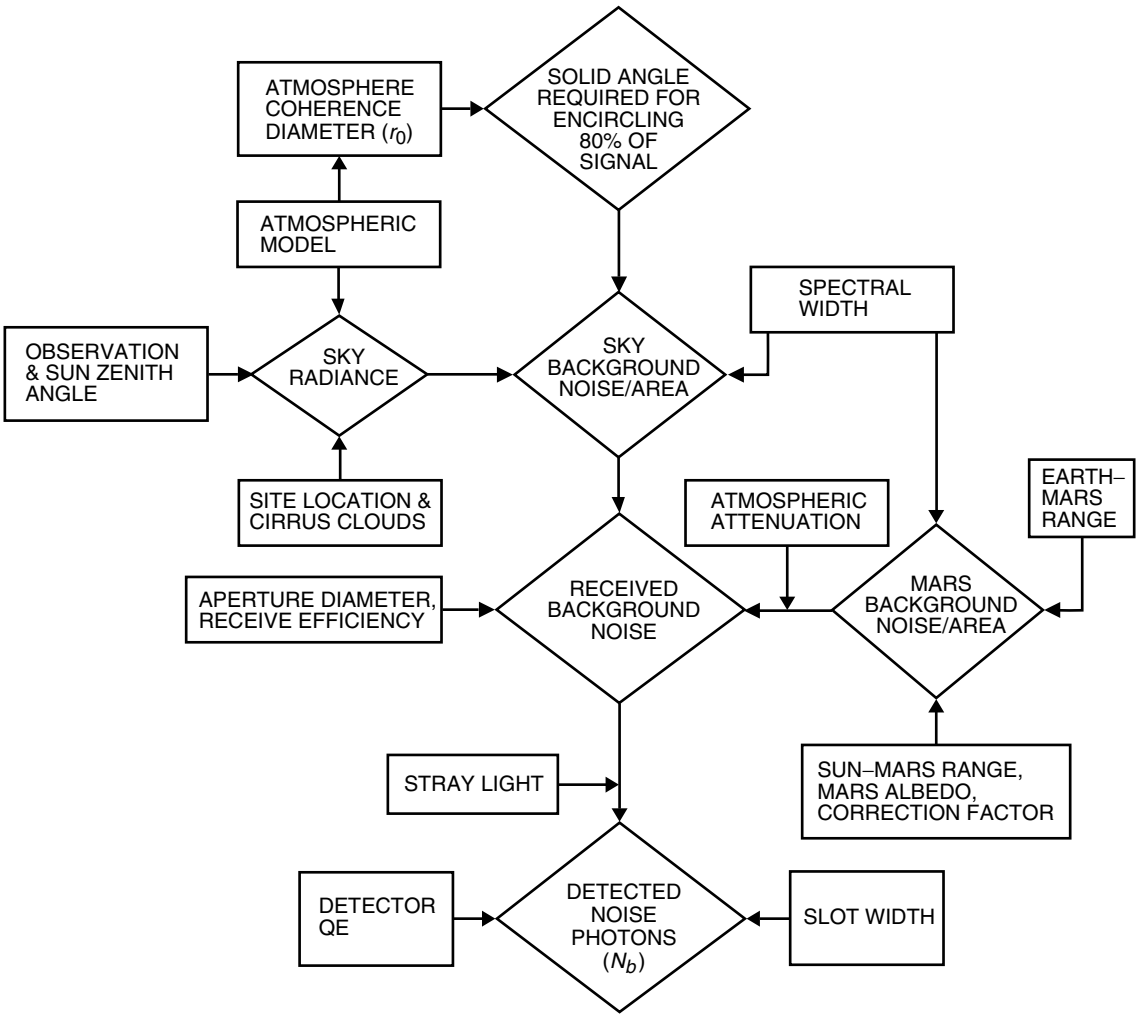

Fig. 12. Flowchart of steps involved in estimating the background noise incident on the detector.

optical collection system with a diffraction-limited focal-spot size of $2.44f\lambda/D$ (with f and D representing the focal length and aperture diameter), the spot size for a beam through atmospheric turbulence, to first order, increases to $2.44f\lambda/r_0$, assuming that the collection aperture diameter $D > r_0$. Not only does atmospheric blurring cause an increase in spot size but the signal is randomly distributed in $(D/r_0)^2$ spatial modes. Each of the spatial modes contributes a fraction of sky noise even though constructive and destructive interference between the signal wave front may cause "hot spots" in some of the modes with depletion of energy in others. However, a single detector used to gather the signal must be sufficiently large to encircle all the spatial modes. This increase in spot size requires a larger detector diameter for collecting the signal, and the two big disadvantages are (1) increased sky background-noise contribution, especially for daytime links, and (2) increased detector capacitance limiting the bandwidth. The large single-detector problem can be circumvented by the use of an array where adaptive processing can be utilized to extract the optimal signal-to-noise ratio with a 3- to 5-dB gain [11] over a single large detector. A second approach would be the use of adaptive optics [12] where reconstruction of the phase results in undoing the blurring. However, the current discussion will proceed to analyze the case for a single large detector.

Consider an ideal annular light collection system with diameter D and obscuration ratio γ. The mean fraction $P(r)$ of the incident energy collected within the normalized detector radius $r \equiv a/\lambda F$ (a is the detector radius, and $F \equiv f/D$) is given by the approximate relation [13]

$$P(r) = 2\pi r \int_0^1 \left\langle \tau\left(\rho,\gamma\right)\right\rangle J1(2\pi r\rho)d\rho \tag{11a}$$

where $\langle\tau(\rho,\gamma)\rangle$ represents the time-averaged optical transfer function (OTF) of the annular optical system, corresponding to a spatial frequency, ρ, with a linear obscuration ratio, γ, and $J1$ is the first-order Bessel function of the first kind. The time-averaged OTF can be expanded further:

$$\left\langle \tau\left(\rho,\gamma\right)\right\rangle = \tau_l(\rho,\gamma)\tau_a(\rho) \tag{11b}$$

Here $\tau_l(\rho,\gamma)$ is the OTF of the aberration-free annular pupil and $\tau_a(\rho)$ represents the effect of turbulence:

$$\tau_a\left(\rho\right) = \exp\left[-3.44\left(\frac{D\rho}{r_0}\right)^{5/3}\right] \tag{11c}$$

where a Kolmogorov model of atmospheric turbulence structure has been used:

$$\tau_l\left(\rho,\gamma\right) = \tau_l(\rho) + \gamma^2\tau_l\left(\rho,\gamma\right) - \tau_{12}(\rho,\gamma) \tag{11d}$$

with

$$\tau_l(\rho) = \frac{2}{\pi(1-\gamma^2)}\left[\cos^{-1}\rho - \rho\left(1-\rho^2\right)^{1/2}\right], \quad 0 \le \rho \le 1 \tag{11e}$$

$$\tau_{12}(\rho,\gamma) = \frac{2\gamma^2}{1-\gamma^2}, \quad 0 \le \rho \le \frac{1-\gamma}{2}$$

$$\tau_{12}(\rho,\gamma) = \frac{2\gamma^2}{1-\gamma^2}\left[1 - \frac{1+\gamma^2}{2\pi\gamma^2}\beta - \frac{1}{\pi\gamma}\sin\beta + \frac{1-\gamma^2}{\pi\gamma^2}\tan^{-1}\left(\frac{1+\gamma}{1-\gamma}\tan\frac{\beta}{2}\right)\right], \quad \frac{1-\gamma}{2} \le \rho \le \frac{1+\gamma}{2}$$

$$\tau_{12}(\rho,\gamma) = 0, \text{ otherwise}$$

$$\beta = \cos^{-1}\left(\frac{1+\gamma^2-4\rho^2}{2\gamma}\right) \tag{11f}$$

In all the equations above, D represents the diameter of the annular pupil with a linear obscuration ratio of γ, and r_0 is the atmospheric Fried parameter. Therefore, assuming Kolmogorov turbulence, the ratio D/r_0 determines the quantity r required to collect a desired fraction of the signal energy, where r is measured in units of λF.

Most reported measurements of r_0 are at wavelengths of 0.5 or 0.3 μm. These r_0 values for zenith measurements were scaled to the optical communications deep-space wavelength of interest, $\lambda = 1.06$ μm, by using a multiplicative factor $(1.06/\lambda)^{1.2}$. This yields zenith-viewing r_0 values in the range of 8.2 to 20 cm for daytime and 12 to 32 cm for nighttime. For a slant range equivalent to a zenith angle of 70 deg, r_0 values can be approximately 50 percent smaller. This yields worst- and best-case r_0 values ranging from 4 to 20 cm for day and 6 to 32 cm for nighttime. Values for r_0 will depend, to a large extent, upon the site location; among other atmospheric parameters, altitude relative to adjacent terrain has a large influence on r_0. Table 7 gives the corresponding D/r_0 values that can be expected for a number of ground antennas.

Figure 13 shows a plot of the integral given by Eq. (11a) for a number of the antennas listed in Table 7. Included in Fig. 13 is a plot for $D/r_0 = 0$, i.e., no atmospheric turbulence. The curve corresponding to $\gamma = 0$ is simply the Airy pattern plot from diffraction theory that shows 84 percent of the energy corresponding to the dimensionless spot size of 1.22 in units of $1/\lambda F$, as expected. As the D/r_0 increases, the mean spot size for encircling a given fraction of energy also increases, as shown in Fig. 13. Figure 13 also shows that a good approximation for the spot size required to encircle 84 percent of the energy is the quantity D/r_0. This approximation gets better as the D/r_0 value increases; for example, for $D/r_0 = 250$ the deviation is <3 percent, while for $D/r_0 = 5$ this increases to 15 percent. Thus, the field of view required for encircling 84 percent of the energy or the ratio of the detector diameter to the focal length is given by

$$FOV_{84\%} \approx \frac{2 \times \dfrac{D}{r_0} \times \lambda F}{f} \approx 2 \times \frac{\lambda}{r_0} \tag{12}$$

The approximation confirms the simple assertion that the half-angle FOV required to collect on an average 84 percent of the signal energy is the atmospheric seeing λ/r_0. Thus, the more severe the turbulence and smaller the r_0, the larger the FOV and corresponding solid angle required to gather 84 percent of the energy. The solid angle is related to FOV by

$$\Omega = 2\pi \left(1 - \cos \frac{\Theta}{2}\right) \tag{13}$$

where Θ is the FOV and can be approximated by $(\pi/4)\Theta^2$ for most cases of interest. Figure 14 shows the same curves as in Fig. 13 with the abscissa scaled in steradians. As expected, the solid angle is

Table 7. Expected D/r_0 values for a number of ground telescopes.

Telescope	D, m	Obscuration, m	Best-day D/r_0	Worst-day D/r_0	Best-night D/r_0	Worst-night D/r_0
Hypothetical	10	1.4	50	250	33	167
Palomar	5	1	25	125	16	83
AEOS	3.67	0.86	18	92	11.5	61
TMF	1	0.2	5	25	17	3

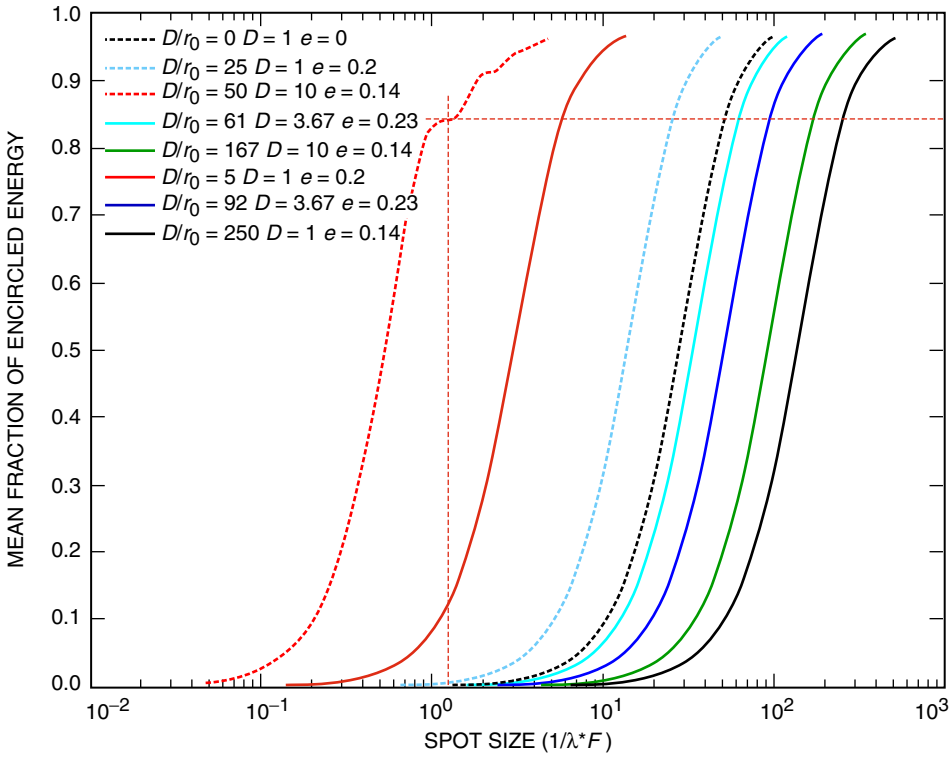

Fig. 13. Dependence of the focal spot size on the atmospheric turbulence represented through the parameter D/r_0 where r_0 represents the atmospheric coherence diameter or Fried parameter.

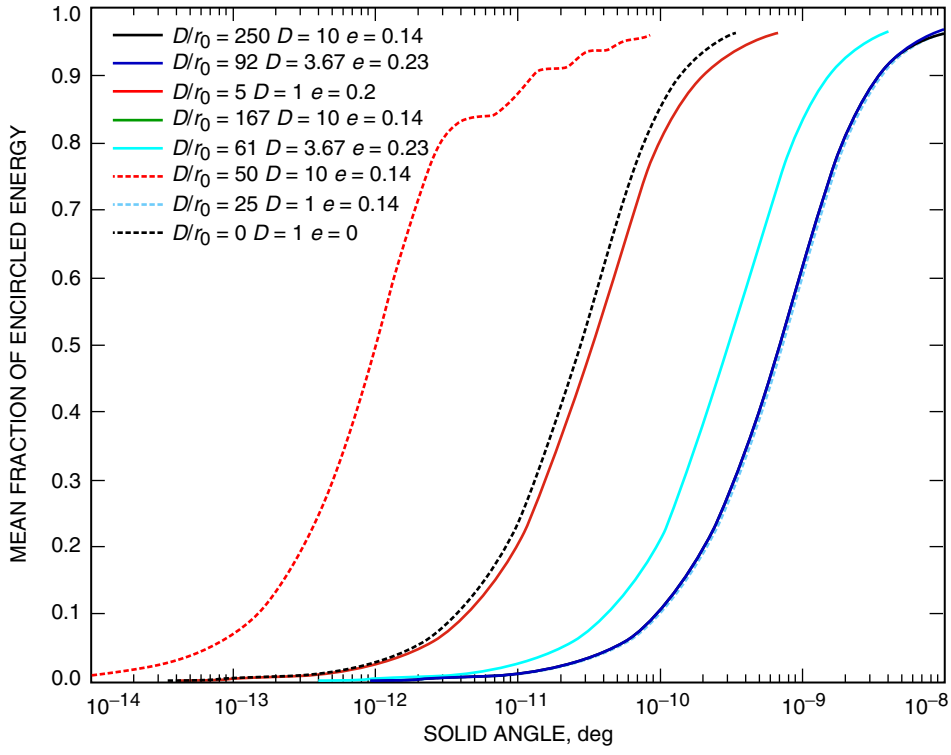

Fig. 14. Same dependence as shown in Fig. 13 with the abscissa rescaled in steradians or solid angle.

determined by r_0 alone; thus, for $D = 10$ or 3.67 m, an $r_0 = 4$ cm results in the D/r_0 ratios being 250 and 92, but the fraction of encircled energy dependence on solid angle is similar. The derivative, or the rate of change in mean encircled energy, is plotted in Fig. 15. For all else remaining the same (see Eq. (16) below), the dependence of noise on solid angle is linear and would appear as a constant level if plotted in Fig. 15. Therefore, depending upon the noise level, the signal-to-noise ratio detected can be optimized by reducing the solid angle on the detector to gather the fraction of encircled energy that maximizes SNR. In the link analysis derived in this article, a 1-dB loss in signal energy is incurred in order to reduce the background without performing the optimization for each situation that may arise.

B. Doppler and Point Ahead

In addition to the spatial modes of sky noise just considered, there are multiple temporal modes determined by the spectral width of the NBPF, expressed either in units of wavelength, $\Delta\lambda$, or frequency, $\Delta\nu$. An important consideration in designing the NBPF is the Doppler shift expected in the laser frequency transmitted from Mars. The Doppler shift is dependent upon the radial velocity between the spacecraft and Earth given by the relation

$$\Delta\nu \approx \nu \frac{V_{\text{radial}}}{c} \tag{14}$$

where $\Delta\nu$ and ν represent the Doppler shift and the laser center frequency, V_{radial} is the radial velocity component between the spacecraft and Earth, and c is the speed of light. For the ground-based receiver,

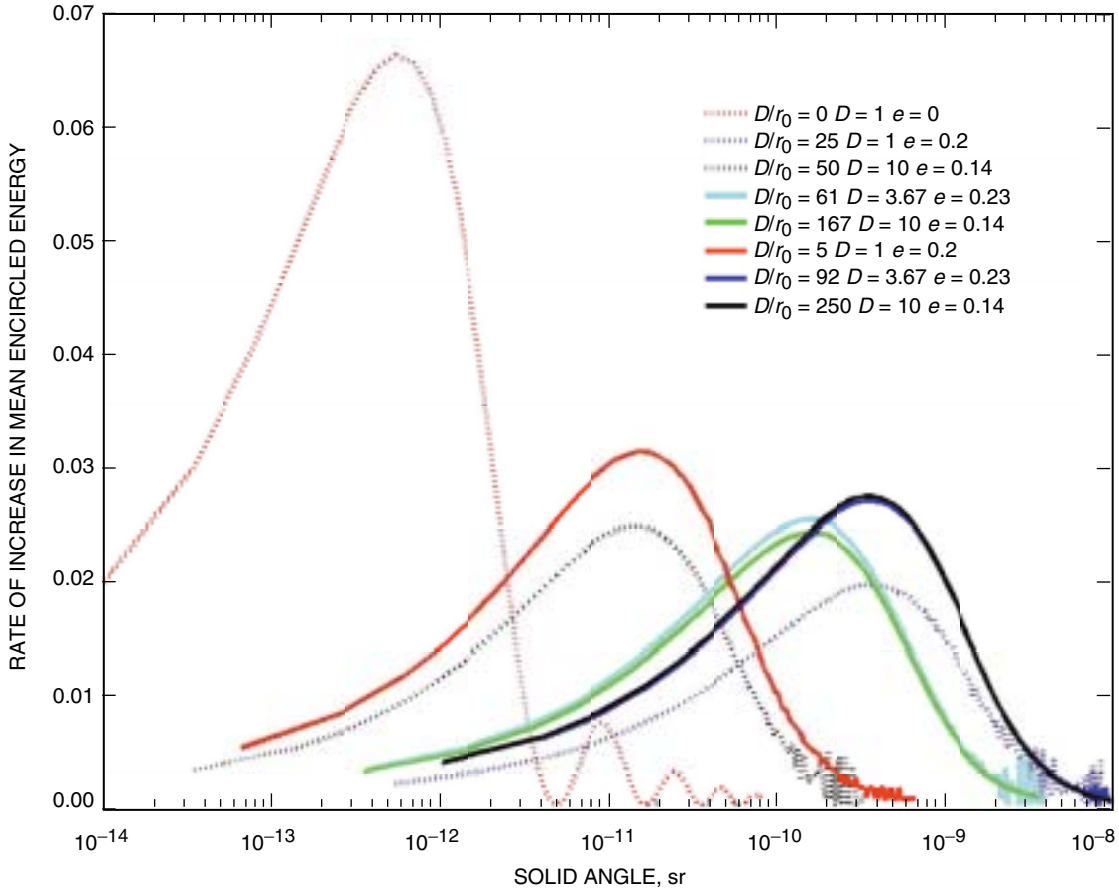

Fig. 15. The rate of change of mean fraction of encircled energy on solid angle for several cases of interest.

Goldstone was used as the receiving station mainly because data relative to Goldstone were available. Figure 16 shows the radial and transverse velocities for the cruise and orbiting phases of a typical Mars mission. Note that the transverse velocity, V_{trans}, translates into point-ahead angle using the relation

$$\Theta_{\text{point-ahead}} = \frac{2V_{trans}}{c} \tag{15}$$

Figures 17 and 18 show plots of the Doppler shifts and point-ahead angles. The maximum radial velocity is of the order of 20 km/s, and the corresponding Doppler shift in frequency is $\Delta\nu = 1.88 \times 10^{10}$ Hz, which corresponds to 0.70 angstroms. For maximum rejection of noise, the filter bandwidth should be narrow; however, if it is made too narrow, then tuning to the line center of the laser beam may prove difficult. To first-order, filter bandwidth sufficiently broader than the laser spectral line width to accommodate the expected drift due to Doppler broadening would be the easiest implementation. Failing this, the capability to tune the filter bandwidth to the line center must be implemented. For the present analysis,

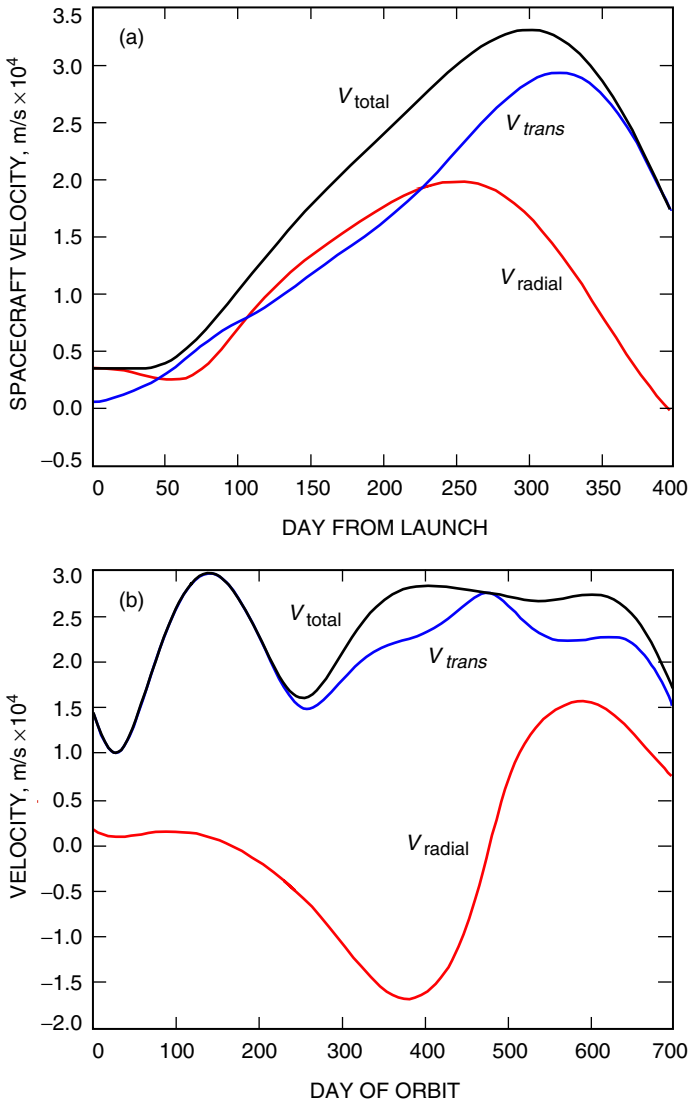

Fig. 16. The radial and transverse velocities derived for (a) the spacecraft during cruise and (b) Mars with respect to Earth after the spacecraft arrives at Mars.

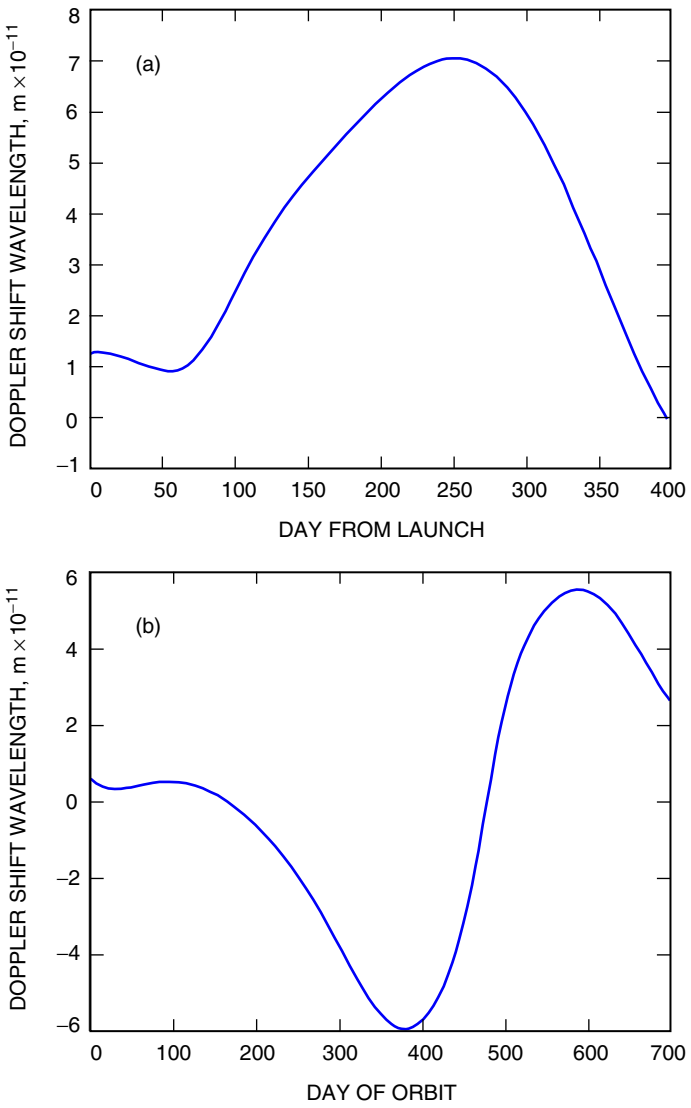

Fig. 17. Doppler shift (a) derived during cruise to Mars and (b) from Mars with respect to Goldstone.

a 1-angstrom (0.1-nm) filter bandpass was selected, and, based upon the Doppler broadening expected, the capability to tune the NBPF for certain durations of the mission when the large Doppler shifts are encountered seems appropriate. The laser line width also would have to be designed to support this scheme.

The spectral line width of the narrow bandpass filter also influences the noise and signal statistics. As shown in [1], a coherent laser signal and broadband background light incident upon a narrowband filter result in a Laguerre probability distribution at the output even though the laser by itself would result in Poisson and the noise by itself would be Bose–Einstein distributed. However, under the valid approximations $T_s B_0 D_s >> 1$ and $(\eta/h\nu)^* N_0 << 1$, the photon statistics can be accurately approximated by the so-called noisy Poisson statistics that are used here. T_s, B_0 and D_s represent slot width in seconds, optical filter bandwidth in Hz, and the number of spatial modes $(D/r_0)^2$, which in our case becomes $2 \times 10^{-9} \times 26.5 \times 10^9 \times (10/0.04)^2 = 3.31 \times 10^6$. N_0 represents the noise per diffraction-limited spatial mode. As shown in the next section, this will rarely be greater than 3×10^{-3} photons/slot, rendering the second approximation above valid.

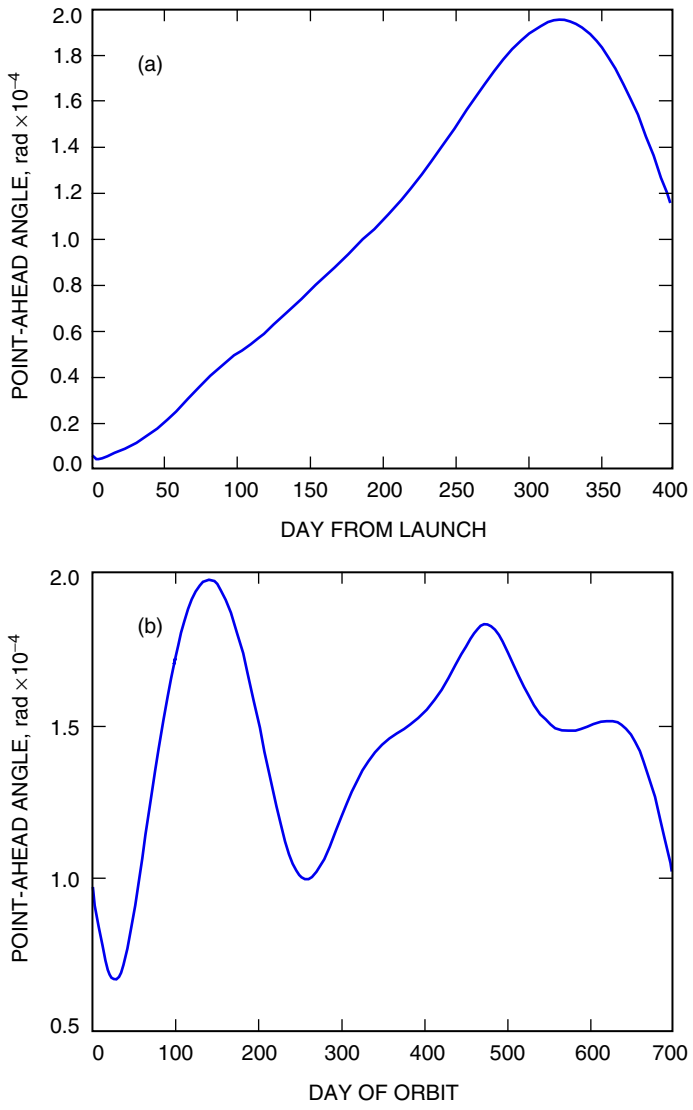

Fig. 18. Point-ahead angle (a) derived during cruise to Mars and (b) at Mars with respect to Goldstone.

C. Sky Radiance Noise

For an Earth-based detector receiving a laser signal transmitted from deep space, the incident background noise photons contributed by sky radiance per PPM-slot time (T_s) is given by

$$n_{b\text{-}skyrad}\left(T_s\right) = \frac{\eta_R^* \pi D^2 \Omega_R \Delta\lambda_{NBPF} L\left(\lambda\right)}{4} \eta_{det} \frac{T_s \lambda}{hc} \tag{16}$$

The receiver system efficiency or optical throughput of the telescope, relay optics, and optical filter combination is η_R^*. Note that η_R^* is different from η_R of Eq. (1). The difference is η_R^* (dB) = (η_{R} − Pol. Loss+3 dB). The assumption is made that the laser signal light is circularly polarized while the noise is not, so that by inserting appropriate polarizing optics at the ground receiver half the background can be rejected. The effective aperture diameter is D, and $\Delta\lambda_{NBPF}$ represents the NBPF optical bandwidth, the same as B_0 above but expressed in angstroms rather than hertz. $L(\lambda)$ represents the sky radiance at

wavelength λ in W/sr cm^2 μm; η_{det} is the detector quantum efficiency; and h and c are Planck's constant and the speed of light.

For a given location on Earth, the sky radiance will depend upon the zenith angle of the Sun, as well as the observation angle with respect to the location of the Sun or the Sun–Earth–probe (SEP) angle. Consider the inverted cone in Fig. 19, with the Sun located along the perimeter of its base and the observer at its apex. The ends of the diametric lines on the base of this cone represent observation zenith angles (ZAs) identical to the Sun, but separated by varying almucantar angles. On the other hand, a principal plane can be defined to include the observer and the Sun, and the observation zenith angle can be varied along this plane to vary the SEP angle. Both the situations described represent variations of SEP, and for a spacecraft the contributions to SEP will be a combination of principal plane and almucantar. In the present analysis, the two types of contributions are treated separately in order to identify bounds on the sky radiance and the resulting background-noise photons.

MODTRAN was used to predict sky radiance with three types of atmospheric models. These were (1) desert extinction with wind speed of 2 m/s, (2) 23-km visibility with no clouds, and (3) 5-km visibility with high cirrus clouds. Note that these assumptions are identical to those used in Table 6 for evaluating atmospheric attenuation. Furthermore, the sky radiance computations were carried out at three different altitudes, namely, sea level, 2 km, and 3 km. The computations of sky radiance with the principal plane assumptions were determined for observation zenith angles ranging from 0 to 70 deg in 10-deg increments. For each observation angle, the Sun position was varied in 5-deg increments from 0 to 85 deg. When the observation and Sun zenith angles coincide, corresponding to looking directly at the Sun, the software cannot compute a sky radiance value. A separation of 0.11 deg was input for these cases. Figures 20 through 22 show a subset of the results of sky radiance for the three different altitudes with all three atmospheric models compared at each altitude. The results are shown as multiple lines plotted as a function of observation angle for a few Sun–zenith angles. Wherever the lines peak corresponds to the observation and Sun–zenith angle being within 0.11 deg.

In order to assess the predictions made by MODTRAN, the sky radiances were compared to data obtained from the NASA Aerosol Robotic Network (AERONET) database. Here raw almucantar and principal plane measurements are reported for globally distributed sites. We used Table Mountain, California, where data were available for a few days in January and February of 2000 to compare with

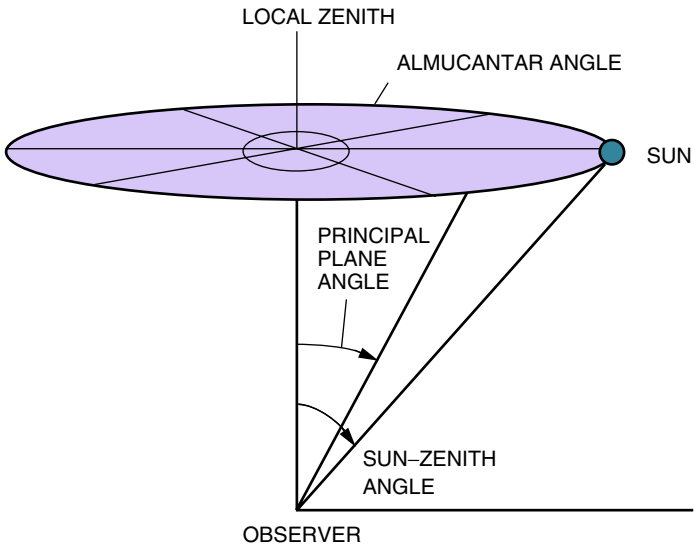

Fig. 19. Sun–observer orientation showing the almucantar and principal plane observation angles.

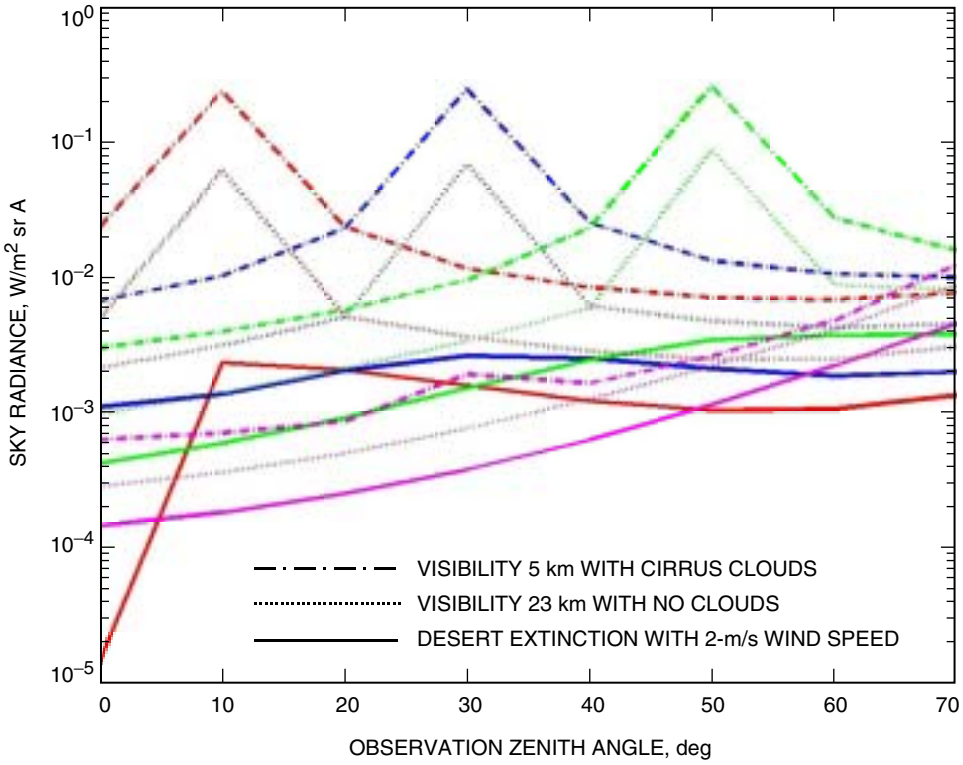

Fig. 20. Sky radiance at sea level for three assumed atmospheric models.

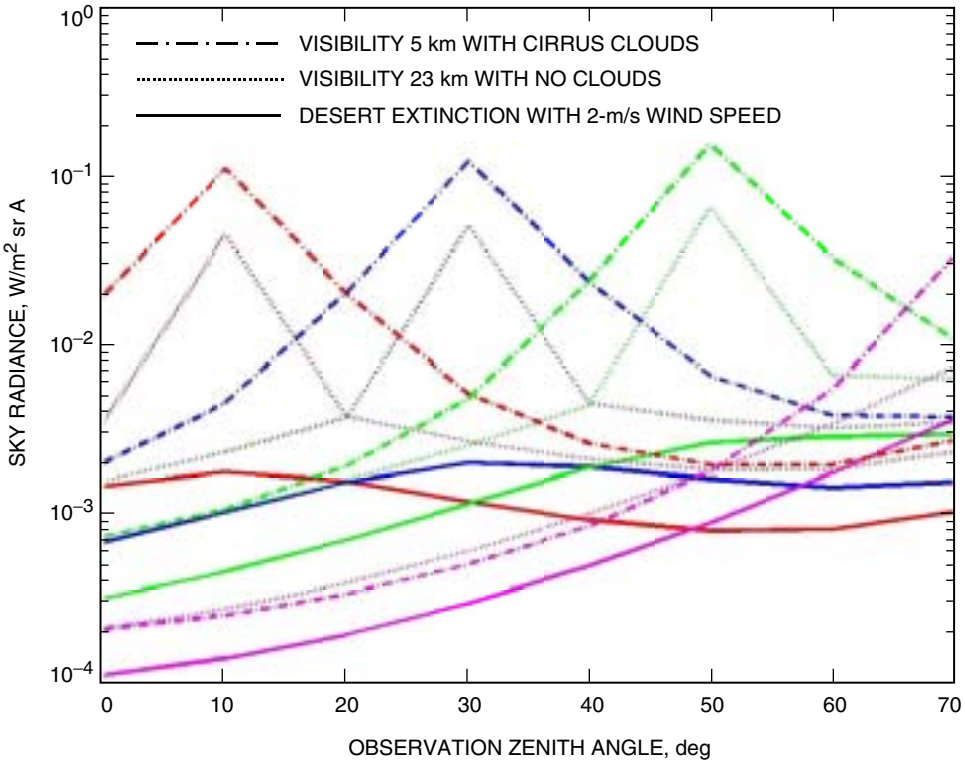

Fig. 21. Sky radiance at 2 km for three assumed atmospheric models.

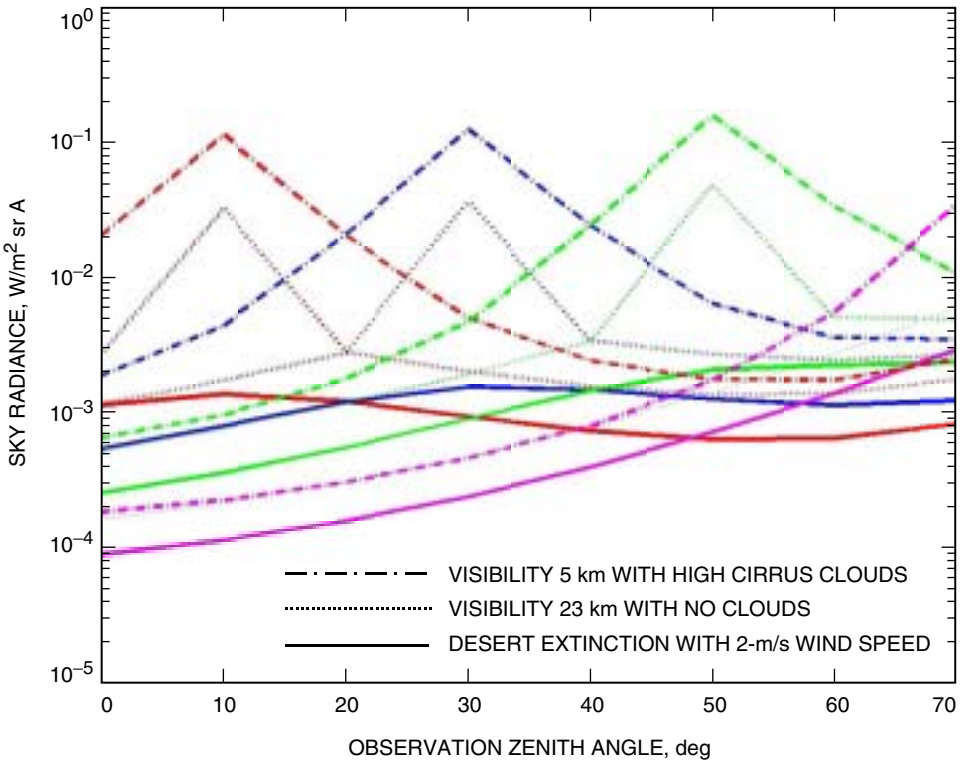

Fig. 22. Sky radiance at 3-km altitude for three assumed atmospheric models.

the 2-km MODTRAN predictions. Figures 23 and 24 show some comparisons for almucantar variations, where the black dots represent the measured sky radiance data points. The red dotted line is the average of all the measurements. For the principal plane data, the MODTRAN predictions also are shown on the same plot. The comparison is shown for a Sun zenith angle of 57 ± 1.5 deg and lends validity to the use of the MODTRAN predictions. Finally, Fig. 25 shows the sky radiance plots of Figs. 21 and 22 translated to the number of background photons per 2-ns slot when using a 10-m-diameter aperture to collect light. For each of the plots in Figs. 21 and 22, Fig. 25 shows the photons over a limited SEP angle range for $r_0 = 4$ and 20 cm. For smaller aperture sizes, all else remaining the same, background photons per slot will scale with collection aperture area.

D. Mars Light

Planets or stars smaller than the detector FOV result in a localized background source on the detector surface. The number of background photons in this case is given by

$$N_{b\text{-}Mars}\left(T_s\right) = \frac{\eta_R^* \pi D^2 \Delta\lambda_{NBPF} I\left(\lambda\right)}{4} \left(alb * F * \eta_{atm} * \eta_{\text{det}}\right) \frac{T_s \lambda}{hc} \tag{17}$$

$I(\lambda)$ is the irradiance from Mars incident at the Earth. The albedo (alb) and a correction factor F that accounts for the dependence of the albedo upon the Sun–probe–Earth angle are used along with the Earth's atmospheric attenuation in order to determine the number of photons contributed by Mars. $I(\lambda)$ is given by

$$I(\lambda) = \left(\frac{H(\lambda)}{R^2_{\text{Sun}-\text{Mars}}}\right)\left(\frac{r_{\text{Mars}}}{Z_{\text{Earth}-\text{Mars}}}\right)^2 \tag{18}$$

where $H(\lambda)$ is the solar irradiance at 1 astronomical unit (au) taken as 668 W/m^2 at 1.064 μm.

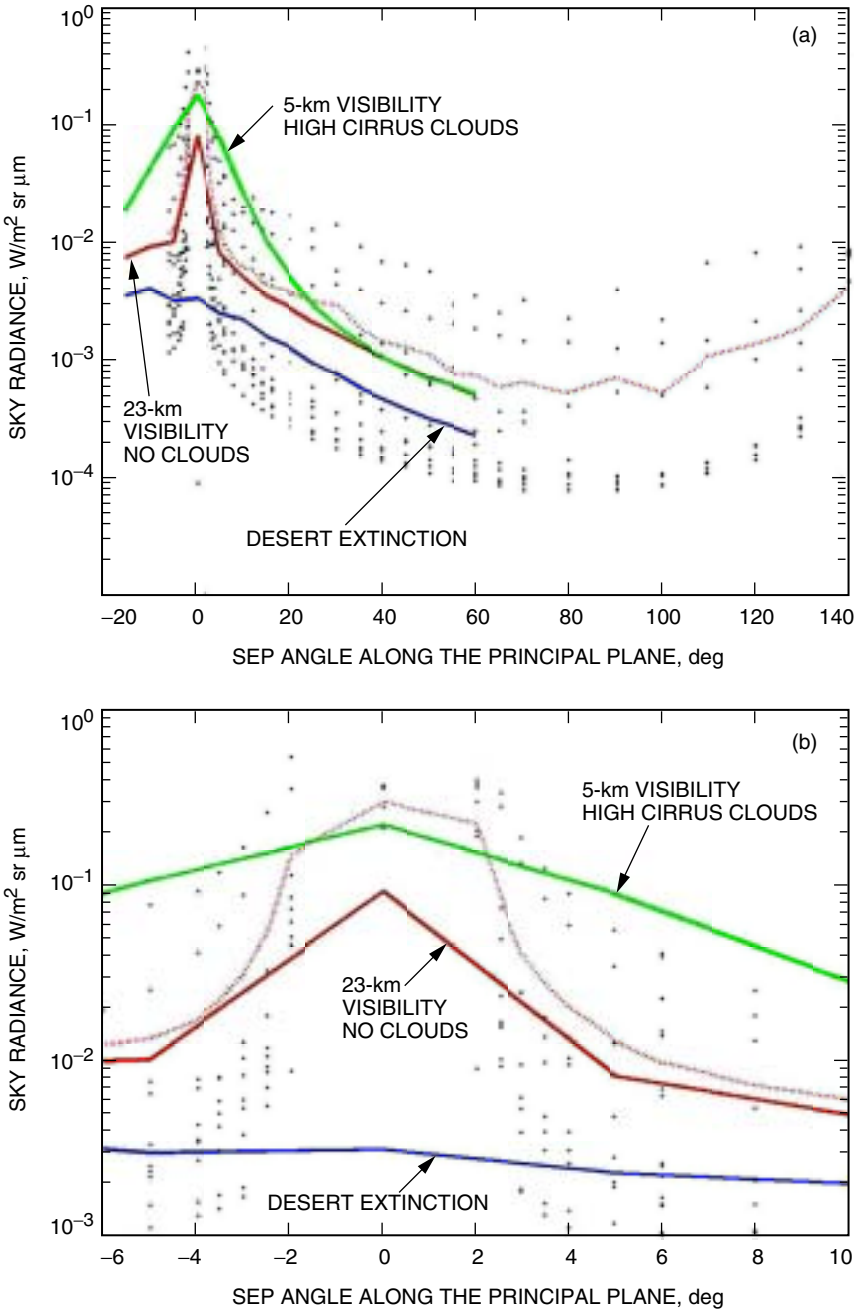

Fig. 23. Comparisons for principal-plane variations: (a) measured sky radiances as a function of SEP angle along the principal plane with the Sun–zenith angle at 57 deg, at Table Mountain, California, for selected days in January and February of 2000 with MODTRAN predictions (solid lines) and the average measured values (dotted line) and (b) a magnified view of Fig. 23 (a) for small SEP angles.

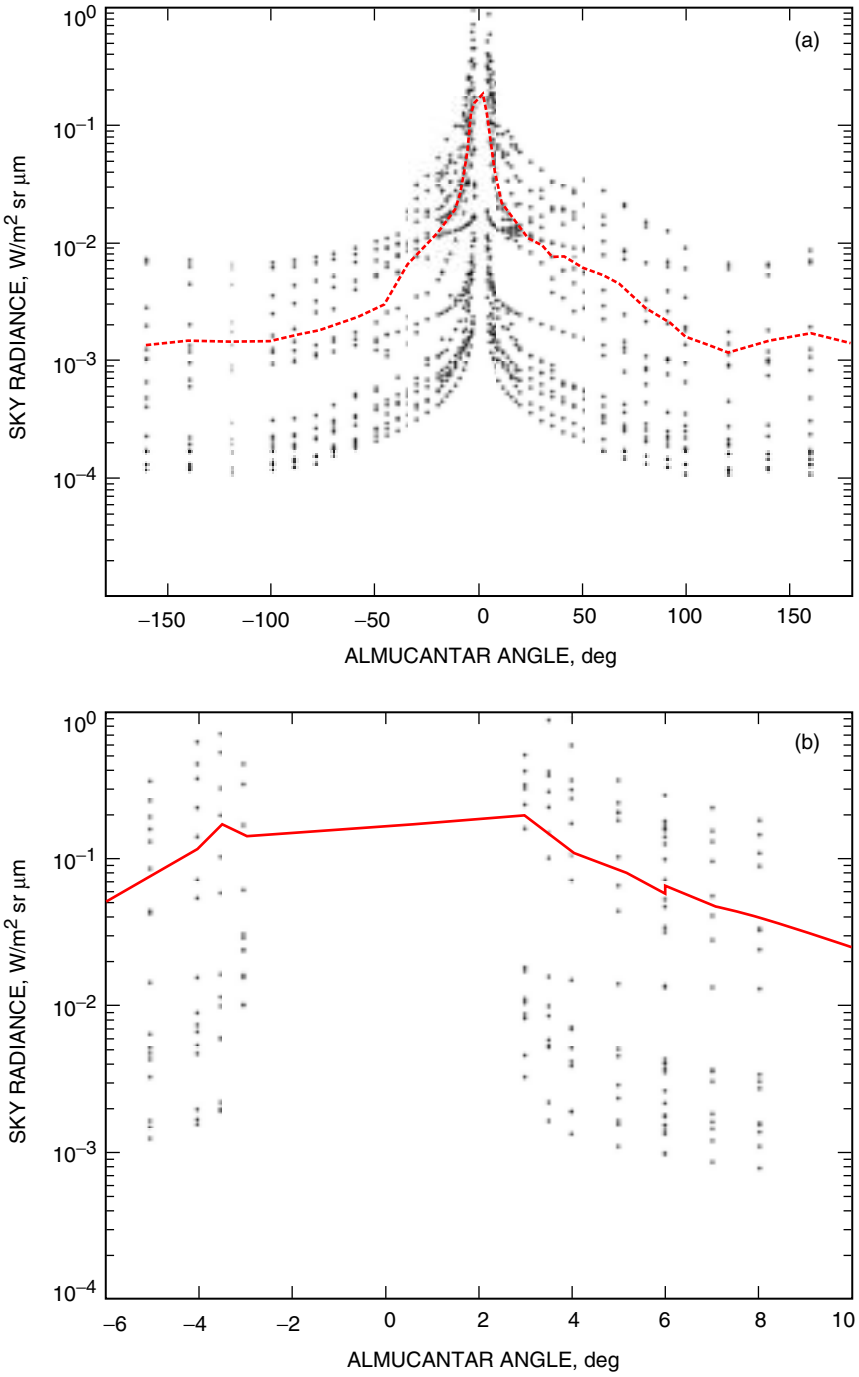

Fig. 24. Comparisons for almucantar variations: (a) sky radiance as a function of almucantar at Table Mountain, California, for a 57-deg Sun–zenith angle measured during selected days in January and February of 2000 and (b) a magnified view of Fig. 24 (a) for small SEP angles.

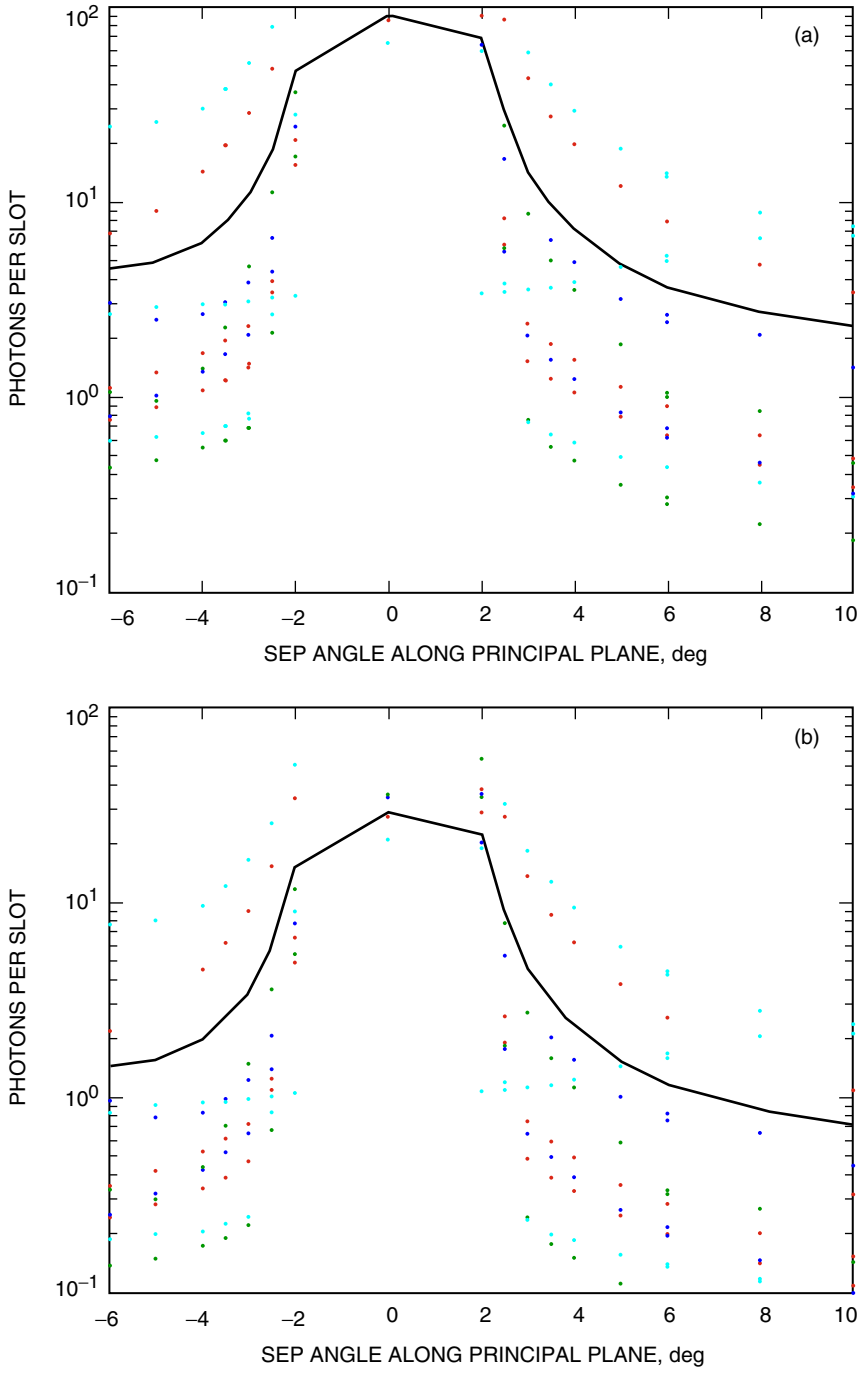

Fig. 25. Background photons at small SEP angles for (a) r_0 = 4 cm, (b) r_0 = 20 cm, (c) r_0 = 4 cm with the almucantar angle shown, and (d) r_0 = 20 cm with the almucantar angle shown. A 10-m-aperture diameter with 1.4-m obscuration, 2-ns slot width, and a 1-angstrom filter is used, and the Sun–zenith angle is 57 deg.

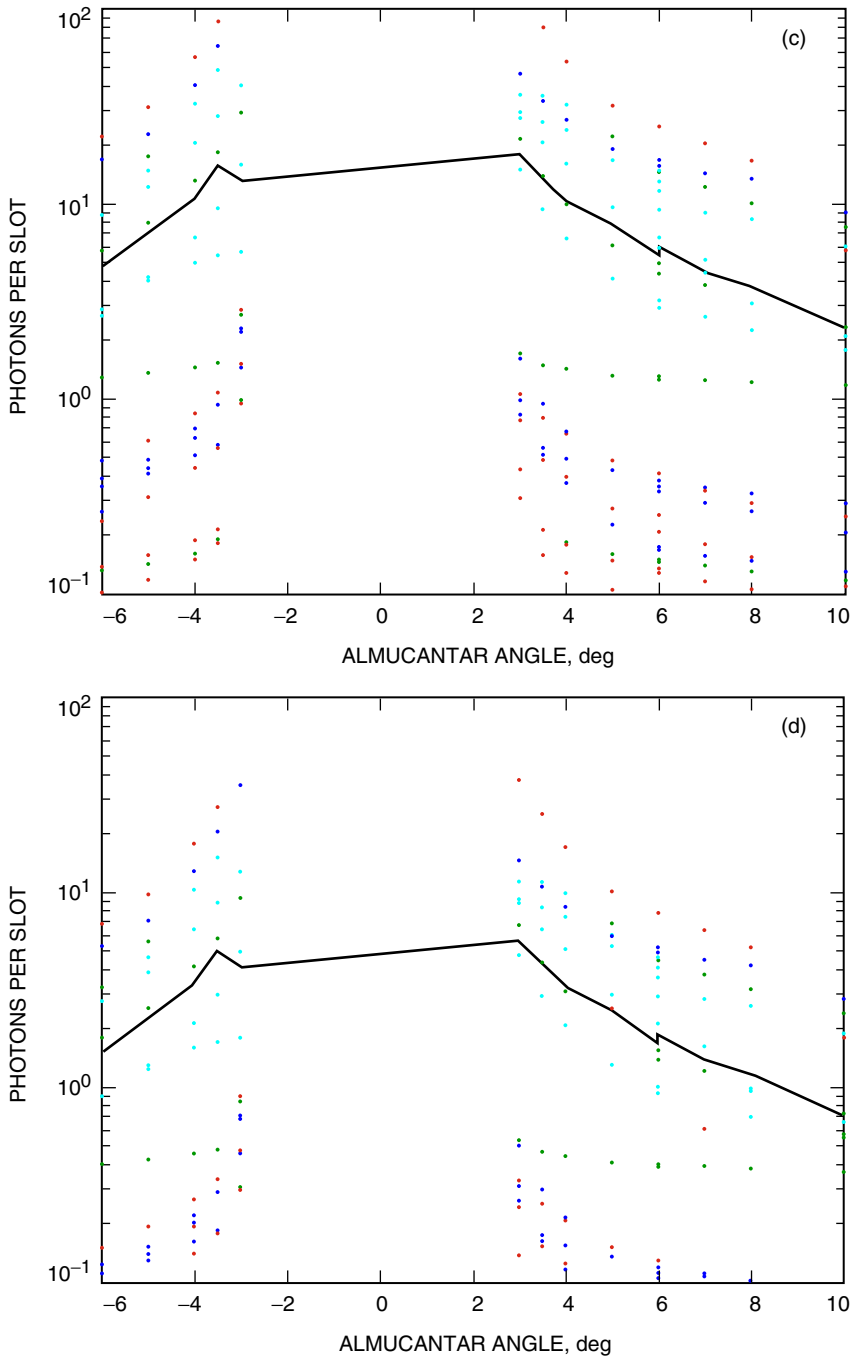

Fig. 25 (contd).

If the angular width of Mars exceeds the detector FOV, then the background photon number estimated using Eq. (17) will be scaled by the ratio of the detector to Mars FOVs. The angular width of Mars varies between 19 and 67 μrad nominally. Median seeing from Palomar, for example, is reported to be 0.9 arcsec or 4.6 μrad with 80 percent of the seeing being better than 8.7 μrad. So, very often the Mars image on the communications detector will be dissected with a corresponding reduction in background-noise photons.

Figure 26(a) shows the dependence of the correction factor on SPE angle. A polynomial fit to this plot is used to determine the correction factor at all SPE angles of interest. The resulting Mars background

photon contribution for a 10-m aperture with a fixed atmospheric attenuation of −1 dB and detector quantum efficiency of 0.46 is shown in Fig. 26(b).

V. Achievable Data Rates

A. Link Budget

In the preceding sections, elements for deriving the number of signal and background-noise photons incident on the detector, using fixed and variable losses, were presented. A design control table (DCT) for a downlink from Mars will be presented in this section, where the average detected signal, n_s/M, and background-noise, n_b, photons are utilized to compute soft-decision capacity using an approach detailed in a companion article [3]. Worst-, nominal-, and best-case allocations of the link budget elements are made in an attempt to establish data rate bounds for the link. As mentioned earlier, a 4.75-dB gap from capacity is assumed in order to identify the realizable data rates. The computation of capacity also provides coding rate and the uncoded symbol-error rates both with margin (SER2) and without margin (SER1).

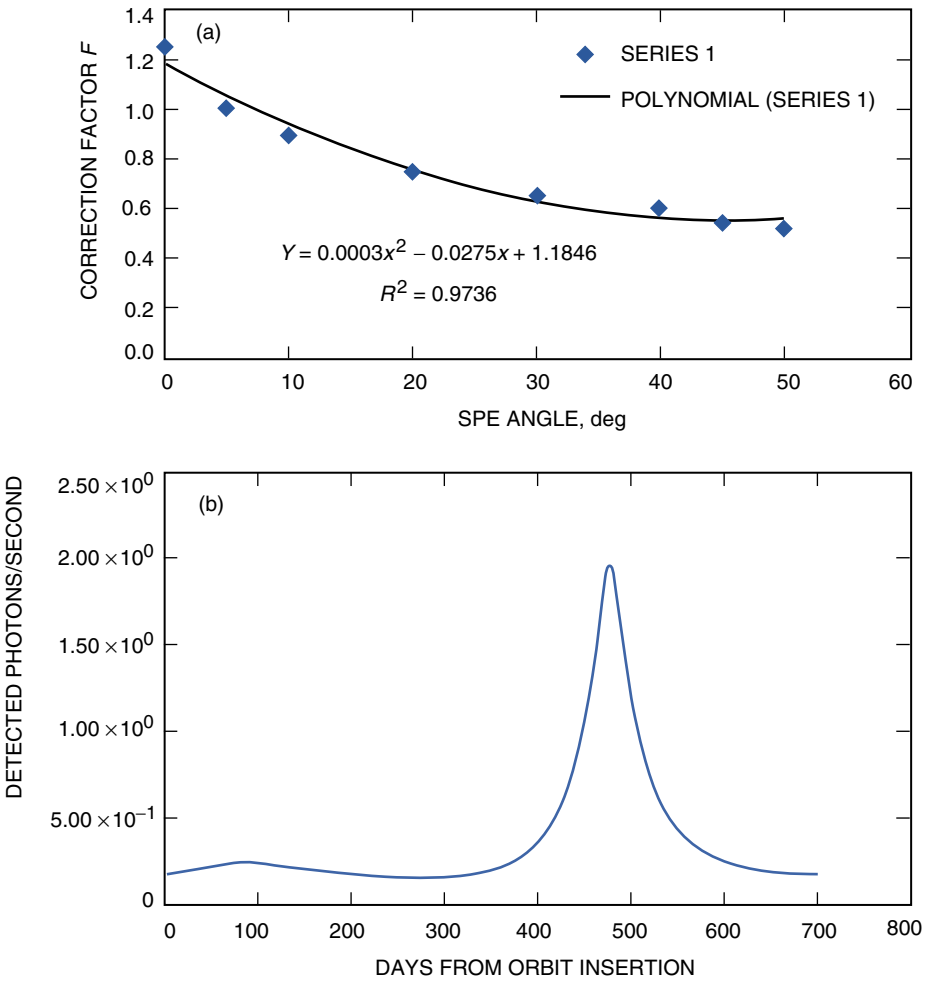

Fig. 26. The variation of Mars' contribution to the detected photons: (a) correction factor to account for Sun illumination angles of Mars and (b) variation of detected photons from Mars; note the peak close to Mars–Earth opposition.

At the time of the writing of this article, reasonable constraint on peak power for a pulsed fiber amplifier laser (currently a strong contender for a Mars downlink transmitter [13]) is 300 to 1500 W.[3] The lower bound of 300 W is based upon the reported peak power achieved for a space-qualified 1550-nm laser flown for the GEOLITE mission. The favored Mars laser wavelength is 1064 nm, where peak power of 1.5 kW is deemed likely.[4] Even though higher peak powers may also be viable (up to tens of kilowatts), we will limit the discussion in this article to an upper bound of 1.5 kW. The peak-power constraint is asserted by setting bounds on the PPM order. Thus, 64- and 256-PPM will correspond to 320 W and 1.28 kW of peak powers.

1. Hypothetical 10-Meter-Aperture-Diameter Receiver Located at 2-Kilometer Altitude. The DCT presented below emphasizes the most stressing case, where Mars is at the farthest range and also closest to the Sun. A 10-m-diameter hypothetical aperture with the ability to point arbitrarily close to the Sun is assumed, for a link estimate with a 3-deg SEP angle. A MATLAB program was used where fixed losses are entered as 3-element vectors for the worst-, nominal-, and best-case assignments. The Mars ephemeris is computed in order to derive the variation of the Mars zenith angle over a typical pass. The 3-deg SEP angle predicted on January 24, 2011, was chosen, and the variations of elevation and azimuth angles (see Fig. 3) were determined assuming the observer to be at the Table Mountain Facility, Wrightwood, California.

Table 8(a) lists the fixed losses based upon the discussions presented in the preceding sections. Note that the receiver losses for the signal and background referred to as η_R and η_R^* in Section III are listed separately in Table 8(a). The example presented uses a PPM slot width of 2 ns and a worst-case photodetection efficiency of 0.4 with a nominal and best-case value of 0.46. Finally, worst atmospheric seeing of 5 arcsec with a nominal value of 1.9 arcsec and best-case value of 0.4 arcsec are assumed; these parameters are listed in Table 8(b).

Based upon the assumptions presented in Tables 8(a) and 8(b), a typical pass of Mars is taken to represent the spacecraft ephemeris on January 24, 2011, when the SEP angle is 3 deg. Table 8(c) tabulates the corresponding parameters. Assuming that Mars is being observed from Table Mountain, California, and that the maximum zenith angle for observing is 70 deg, the Pacific Standard Time (PST) for Mars to rise with hourly updates on elevation angle until it sets are given in the first two columns of Table 8(c). The corresponding space loss and worst, nominal, and best atmospheric attenuation are tabulated next. These variable terms are used to estimate the net signal photons that can be detected

Table 8(a). DCT showing fixed gain/loss allocations.

Fixed allocations (losses and gains)	Worst, dB	Nominal, dB	Best, dB
Transmit losses	−2.34	−1.86	−1.43
Transmitter gain	116.8	117.3	117.8
Pointing loss	−2.00	−1.61	−1.25
Signal receive loss	−5.58	−5.05	−4.58
Receiver gain	149.1	149.2	149.3
System fixed loss for signal	256	257.98	259.84
Background receive loss	−8.38	−6.3	−5.02

[3] M. Wright, personal communication with Y. Deiss, Keopsys, Lannion, France.

[4] *Mars Lasercom Study,* Phase II Readout, Lincoln Laboratory, Massachusetts Institute of Technology, Lexington, Massachusetts, May 29, 2003.

Table 8(b). Link parameters used for deriving DCT allocations.

Additional link parameters	Worst	Nominal	Best
Sky radiance from MODTRAN, W/m^2 sr A	0.003	0.064	0.174
Sky radiance from AERONET, W/m^2 sr A	0.004	0.009	0.096
Photo-detection efficiency	0.40	0.46	0.46
Slot width, ns	2.00	2.00	2.00
Atmospheric seeing, arcsec	5	1.9	0.4

Table 8(c). Derived signal and noise photons received using a 10-m-diameter aperture, with a 0.1-nm optical filter, as a function of elevation angle for a representative pass close to Earth–Mars conjunction.

Time, PST	Mars elevation, deg	Space loss, dB	Atmospheric attenuation			Average signal (n_s/M)			Background noise (n_b)		
			Worst, dB	Nominal, dB	Best, dB	Worst	Nominal	Best	Worst	Nominal	Best
9:00	24	−372.47	−2.0	−0.5	−0.4	0.031	0.078	0.125	19.85	0.86	0.09
10:00	32	−372.47	−1.5	−0.4	−0.3	0.034	0.081	0.127	15.12	0.48	0.06
11:00	37	−372.47	−1.3	−0.4	−0.3	0.035	0.081	0.128	3.16	0.34	0.04
12:00	38	−372.47	−1.3	−0.4	−0.3	0.036	0.082	0.129	3.16	0.30	0.04
13:00	36	−372.47	−1.4	−0.4	−0.3	0.035	0.081	0.128	5.01	0.34	0.05
14:00	30	−372.47	−1.6	−0.4	−0.3	0.033	0.080	0.127	0.90	0.52	0.07
15:00	21	−372.47	−2.2	−0.6	−0.5	0.029	0.077	0.123	19.85	0.85	0.09

at the focal plane of a hypothetical 10-m aperture. Next the background photons contributed by the sky and Mars are estimated, while stray light has not been considered. In [8], analysis was presented to introduce the concept that a ground receiver could be designed so that at shallow SEP angles (<10 deg) the stray-light contribution could be limited to a factor of 2 of the background sky noise received when looking away from the Sun. For estimating background noise, both MODTRAN predicted values as well as values obtained from the AERONET data base were used; the actual values are given in Table 8(b).

Combining the best of the best and worst of the worst cases for the background yields the background photons per slot listed in Table 8(c). This approach yields background photon estimates that vary by 2 to 3 orders of magnitude. This scheme of combining the worst sky radiance and worst seeing is questionable, however, because it provides no idea of the statistical probability of obtaining a combination of the worst-case conditions. In order to explore this further, the statistical distribution of daytime seeing together with statistical distribution of sky radiance is required. At the time of the writing of this article, access to simultaneously gathered seeing and radiance data from a single site was not available; however, daytime solar seeing data [14] from Sacramento Peak, New Mexico, and AERONET sky radiance data from Table Mountain, California, were available. These data sets are shown in Fig. 27. Figure 28 shows the cumulative probability distribution of background photons per slot derived by combining these distributions and assuming to first order that the sky radiance and seeing are uncorrelated. From Fig. 28, it is apparent that the instances of the very high background predicted in Table 8(c) are present but a negligibly small fraction of the time. The nominal values of 0.3 to 0.5 occur only 3 to 4 percent of the time whereas 0.05 to 0.09 (best) occurs 75 percent or less of the time. Thus, combining the worst of the worst backgrounds provides a skewed representation of the signal and noise distributions. The cumulative probability distribution of Fig. 28 does not necessarily provide the correct estimate of background photons

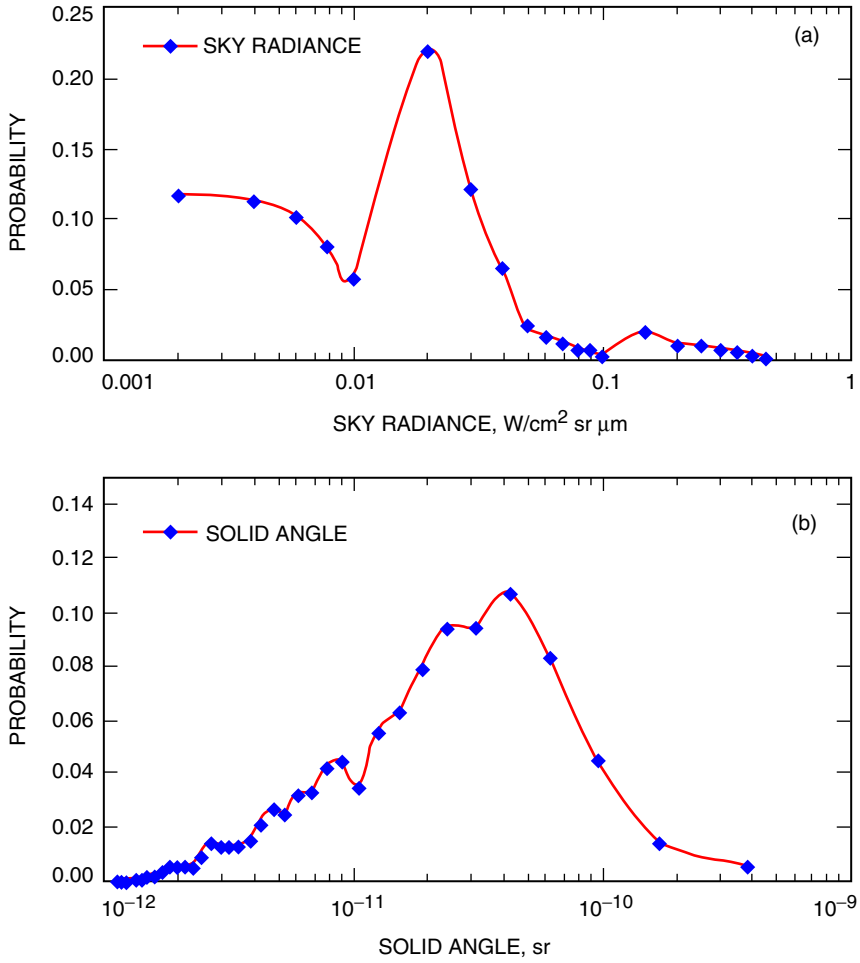

Fig. 27. Daytime atmospheric data: (a) statistical distribution of sky radiance observed at Table Mountain, California, during June and July of 2003 and (b) 2-year statistics of daytime seeing at Sacramento Peak, New Mexico.

because two different sites are being compared; however, the technique of combining sky radiance and seeing data is being emphasized. One of the recommendations apparent from the work reported here is the importance of acquiring simultaneous sky-radiance and seeing data to get a realistic estimate of the levels of background that daytime optical links will have to contend with.

Based upon the preceding discussion, we select a subset of n_s/M and n_b pairs for capacity computations, shown in Table 9. Thus, the best, nominal, and worst results for n_s/M from Table 8(c) are chosen, but for n_b the numbers 0.05, 0.2, and 0.8, representing the 60th, 95th, and 99th percentile occurrences predicted by combining sky radiance data from Table Mountain, California, and seeing data from Sacramento Peak, New Mexico, are taken. The computations are then carried out to determine what M provides the optimal data rate given the average signal and noise photons predicted. Thus, the first results tabulated in Table 9 impose an upper bound of $M = 256$ and a lower bound of $M = 64$. The capacity and bits per slot take into account the 4.75-dB gap mentioned earlier. According to the idealized Poisson channel capacity calculations, data rates ranging from 5.52 to 40 Mb/s can be achieved. A few other link parameters are also shown, such as the code rates and uncoded symbol-error rates (SERs). The symbol-error rates are generally high, especially for the worst case considered. The average number of detected photons per pulse varies from 5 to 8. The coding strategy [3] is such that high SERs are acceptable and can be reduced to $<10^{-6}$ bit-error rate (BER).

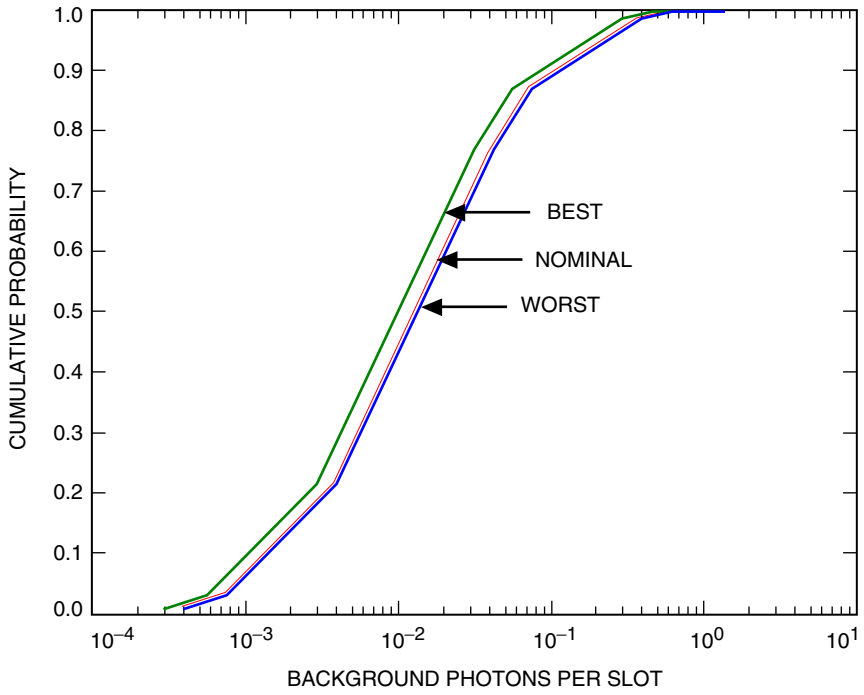

Fig. 28. The cumulative distribution of background photons per slot derived using the statistical distributions of Fig. 27 and assuming that sky radiance and seeing are uncorrelated.

Table 9. Summary of derived data rates based on a 0.75-dB gap from channel capacity.

Results	$M = 256$ maximum and $M = 64$ minimum											
	n_s/M	n_b	M	d	Capacity, b/slot	Data rate, Mb/s	Code rate	SER	PRF, Hz	E_p, J	Pk_{Pwr}, W	Average detected photon/ pulse
Worst	0.03	0.9	256	0	0.01103	5.52	0.35	0.65	2.0×10^6	2.6×10^{-6}	1.3×10^3	8
Nominal	0.08	0.2	64	0	0.0444	22.20	0.47	0.46	7.8×10^6	6.4×10^{-7}	3.2×10^2	5
Best	0.13	0.05	64	0	0.07905	39.53	0.84	0.13	7.8×10^6	6.4×10^{-7}	3.2×10^2	8

There is concern, however, with regard to the synchronization algorithms being able to achieve slot synchronization when the uncoded SERs are high. This will be the subject of future articles and will not be addressed here.

VI. Conclusions

A preliminary systems analysis for an optical link from Mars has been presented. The analysis emphasizes the atmospheric contributions to system background noise that have a very serious impact on the link performance. The results suggest that the 10-Mb/s target for Mars at the farthest range with the associated minimum SEP angle of 3 deg appear achievable. A definite assessment requires further work in several areas.

Statistical models that describe the atmospheric impact of seeing and sky radiance at potential receiving sites need to be better understood. Moreover, the same approach taken with sky radiance and seeing can be adapted for seeing and atmospheric attenuation in order to get a probabilistic estimation of Mars' noise contribution, which becomes more significant as Mars gets closer to Earth.

Neglect of the stray light in the analysis will have a small effect on the predictions, assuming the assumptions alluded to in [8] can be met in a designed large-aperture optical receiving antenna.

The synchronization algorithms and their tolerance to high symbol-error rates are areas that need to be properly addressed. Preliminary analysis, to be reported upon soon, indicates that SER = 0.4 may be a reasonable upper bound, with SER = 0.1 being a very low risk target.

The effect of realistic device constraints on the laser and detector will also take some performance away from the predictions made here. For example, no dead time has been assumed for the laser. With the advent of space-qualifiable fiber amplifier lasers, this may not be entirely unrealistic; however, even with these lasers, obtaining consecutive pulses from the last slot of one PPM symbol and the first slot of the next consecutive symbol will most likely result in a reduction of peak power that is not accounted for here. Likewise, realistic detector noise and variability in performance will also cost 3 to 4 dB, as will be documented in upcoming articles.

Given all the persisting uncertainties, it would certainly not be unrealistic to expect 10-Mb/s data rates from the farthest distance to Mars. The question is what fraction of the time will this be achievable. Moreover, the analysis presented also can be used to improve the designs of some parameters so as to increase the viability of attaining the 10-Mb/s objective. For example, the spectral width of the narrow bandpass optical filter certainly can be reduced by a factor of 4 to 5 while simultaneously developing strategies for actively tuning the filter to the Doppler-shifted laser peak wavelength; this will largely mitigate the background-noise problem.

In conclusion, the basic developments required to establish optical links from Mars need to be tested out, as the planned Mars Laser Communications Demonstration currently plans to do. With the basic validation accomplished, many refinements to improve and provide robust deep-space links will become feasible.

References

[1] R. M. Gagliardi and S. Karp, *Optical Communications,* 2nd ed., New York: John Wiley & Sons, p. 203, 1995.

[2] J. Hamkins, "The Capacity of Avalanche Photodiode-Detected Pulse-Position Modulation," *The Telecommunications and Mission Operations Progress Report 42-138, April–June 1999,* Jet Propulsion Laboratory, Pasadena, California, pp. 1–19, August 15, 1999.
http://tmo.jpl.nasa.gov/tmo/progress_report/42-138/138A.pdf

[3] B. Moision and J. Hamkins, "Downlink Budget for Mars: Modulation and Coding," *The Interplanetary Network Progress Report 42-154, April–June 2003,* Jet Propulsion Laboratory, Pasadena, California, pp. 1–28, August 15, 2003.
http://ipnpr.jpl.nasa.gov/progress_report/42-154/154K.pdf

[4] B. J. Klein and J. J. Degnan, "Optical Antenna Gain 1: Transmitting Antennas," *Applied Optics,* vol. 13, pp. 2134–2140, 1974.

[5] V. N. Mahajan, "Aberration Theory Made Simple," Series Ed., D. O' Shea, vol. TT-6, Bellingham, Washington: SPIE Optical Engineering Press, p. 74, 1991.

[6] V. A. Vilnrotter, "The Effects of Pointing Errors on the Performance of Optical Communications Systems," *The Telecommunications and Data Acquisition Progress Report 42-63, March and April 1981,* Jet Propulsion Laboratory, Pasadena, pp. 136–146, June 15, 1981.
http://tmo.jpl.nasa.gov/tmo/progress_report/42-63/63S.PDF

[7] J. J. Degnan and B. J. Klein, "Optical Antenna Gain 2: Receiving Antennas," *Applied Optics,* vol. 13, pp. 2397–2401, 1974.

[8] M. Britcliffe, D. Hoppe, W. Roberts, and N. Page, "A Ten-Meter Ground-Station Telescope for Deep-Space Optical Communications: A Preliminary Design," *The InterPlanetary Network Progress Report 42-147, July–September 2001,* Jet Propulsion Laboratory, Pasadena, California, pp. 1–17, November 15, 2001.
http://ipnpr.jpl.nasa.gov/tmo/progress_report/42-147/147G.pdf

[9] A. Berk, G. P. Anderson, P. K. Acharya, J. H. Chetwynd, L. S. Bernstein, E. P. Shettle, M. W. Matthew, and S. M. Adler-Golden, *MODTRAN User's Manual,* Air Force Research Laboratory, Space Vehicle Directorate, Air Force Materiel Command, Hanscom AFB, Massachusetts, August 1999.

[10] D. L. Fried, "Optical Resolution through a Randomly Inhomogeneous Medium," *Journal of Optical Society of America,* vol. 56, pp. 1372–1379, 1965.

[11] V. A. Vilnrotter and M. Srinivasan, "Adaptive Detector Arrays for Optical Communications Receivers," *IEEE Transactions on Communications,* vol. 50, issue 7, pp. 1091–1097, July 2002.

[12] K. E. Wilson, N. Page, J. Wu, and M. Srinivasan, "The JPL Optical Communications Laboratory Test Bed for the Future Deep Space Optical Network," *The Interplanetary Network Progress Report 42-153, January–March 2003,* Jet Propulsion Laboratory, Pasadena, California, pp. 1–12, May 15, 2003.
http://ipnpr.jpl.nasa.gov/progress_report/42-153/153G.pdf

[13] V. N. Mahajan and B. K. C. Lum, "Imaging through Atmospheric Turbulence with Annular Pupils," *Applied Optics,* vol. 20, pp. 3233–3237, 1981.

[14] P. N. Brandt, H. A. Mauter, and R. Smartt, "Dsy-Time Seeing Statistics at Sacramento Peak Observatory," *Astronomy and Astrophysics,* vol. 188, pp. 163–168, 1987.